

A geostatistical approach to map near-surface soil moisture through hyper-spatial resolution thermal inertia

Antonio Paruta, Giuseppe Ciralo, Fulvio Capodici, Salvatore Manfreda, Silvano Fortunato Dal Sasso, Ruodan Zhuang, Nunzio Romano, Paolo Nasta, Eyal Ben-Dor, Nicolas Francos, Yijian Zeng and Antonino Maltese

Abstract— Thermal inertia has been applied to map soil water content exploiting remote sensing data in the short and long wave regions of the electromagnetic spectrum. Over the last years, optical and thermal cameras were sufficiently miniaturized to be loaded onboard of Unmanned Aerial Systems (UASs), which provide unprecedented potentials to derive hyper-spatial resolution thermal inertia for soil water content mapping. In this study, we apply a simplification of thermal inertia, the apparent thermal inertia (*ATI*), over pixels where underlying thermal inertia hypotheses are fulfilled (unshaded bare soil). Then, a kriging algorithm is used to spatialize the *ATI* to get a soil water content map. The proposed method was applied to an experimental area of the Alento River catchment, in southern Italy. Day-time radiometric optical multispectral and day and night -time radiometric thermal images were acquired via a UAS, while in-situ soil water content was measured through the thermo-gravimetric and Time Domain Reflectometry (TDR) methods. The determination coefficient between *ATI* and soil water content measured over unshaded bare soil was 0.67 for the gravimetric method and 0.73 for the TDR. After interpolation, the correlation slightly decreased due to the introduction of measurements on vegetated or shadowed positions ($r^2 = 0.59$ for gravimetric method; $r^2 = 0.65$ for TDR). The proposed method shows promising results to map the soil water content even over vegetated or shadowed areas by exploiting hyper-spatial resolution data and geostatistical analysis.

Index Terms—Variogram analysis, kriging interpolation, UAS, Thermal admittance, Thematic mapping.

I. INTRODUCTION

SOIL WATER CONTENT is defined as the amount of water on a volumetric basis contained in a specific volume of soil, θ ($\text{m}^3 \text{m}^{-3}$) [1], and is one of the most important hydrologic state variables as it affects the dynamics of many processes occurring in different environmental systems such as run-off generation, evapotranspiration, irrigation, and drainage. Also, this variable plays a key role in understanding and tackling many problems such as flash-flood alerting and landslide predictions [2].

Two widespread methods to determine point-based θ values are the thermo-gravimetric method and Time Domain Reflectometry (TDR) (a list of the acronyms used in this manuscript is reported in the appendix, Table A1). The former is a direct method and considered as a reference to obtain accurate and precise θ values. The thermo-gravimetric method is relatively simple to be implemented, but requires the collection of undisturbed soil cores, which makes it rather time-consuming especially if one is interested in characterizing the θ space-time variability. The TDR method is an indirect one as it measures the apparent soil dielectric permittivity from which θ is estimated through an empirical calibration equation. Two main advantages make this indirect method particularly attractive for field measurements: *i*) the relative ease in determining near-surface θ values during field campaigns, and *ii*) the fact that TDR measures the apparent dielectric permittivity as active microwave sensors placed on aircrafts or satellites do.

Both the thermo-gravimetric and TDR methods have some drawbacks that confine their use when mapping soil moisture over relatively large areas. TDR can provide measurements with a good temporal resolution, but it is limited in spatial resolution and extent. Thus, it is still not operationally feasible to extend TDR measurement network to provide measures at

Manuscript received ...; revised ...; accepted This research was funded by COST Action CA6219 - Harmonization of UAS techniques for agricultural and natural ecosystems monitoring (*Corresponding author: Antonino Maltese*).

A. Paruta (A.P.), G. Ciralo (G.C.), F. Capodici (F.C.) and A. Maltese (A.M.) are with the Department of Engineering, Università degli Studi di Palermo, Palermo, Italy (e-mail: antonio.paruta@community.unipa.it, giuseppe.ciralo@unipa.it, fulvio.capodici@unipa.it, antonino.maltese@unipa.it).

S. Manfreda (S.M.) is with the Department of Civil, Architectural and Environmental Engineering, University of Naples Federico II, via Claudio 21, 80125 Napoli, Italy (e-mail: salvatore.manfreda@unina.it).

S. F. Dal Sasso (S.F.D) and R. Zhuang (R.Z.) are with the Department of European and Mediterranean Cultures, Architecture, Environment, Cultural

Heritage, University of Basilicata, 75100 Matera, Italy (e-mail: silvano.dalsasso@unibas.it, ruodan.zhuang@unibas.it).

N. Romano (N.R.) and P. Nasta (P.N.) are with the Department of Agricultural Sciences, AFBE Division, University of Naples Federico II, Portici (Napoli), Italy (e-mail: nunzio.romano@unina.it, paolo.nasta@unina.it)

E. Ben-Dor (E.B.) and N. Francos (N.F.) are with the Department of Geography and Human Environment, Tel Aviv University, Israel (e-mail: bendor@post.tau.ac.il, nicolasf@mail.tau.ac.il).

Y. Zeng (Y.Z.) is with the Department of Water Resources, ITC Faculty of Geo-Information Science and Earth Observation, University of Twente, Enschede, the Netherlands (e-mail: y.zeng@utwente.nl)

Digital Object Identifier ...

the catchment scale (*e.g.*, $\sim 10^1\text{--}10^2\text{ km}^2$) [3], and at the same time, maintain the measurement grid resolution at plot scale (sub-meter).

On the other hand, although the thermo-gravimetric method allows achieving higher accuracies when compared with the TDR technique, collecting undisturbed soil cores (even if from the uppermost soil horizon) is rather prohibitive depending on the area morphology and/or if sampling a large number of positions is needed.

To estimate the spatial distribution of θ , the research community developed new approaches based on remotely sensed data acquired in different regions of the electromagnetic spectrum, including microwave, shortwave and longwave. For example, both active and passive microwaves images can be used to estimate near-surface θ , as described in the reviews of Sabaghy *et al.* [4] and Barrett *et al.* [5]. Regarding active microwaves, a list of several Synthetic Aperture Radar (SAR) approaches is reported in Capodici *et al.* [6] that classified several previous studies in terms of: *i*) frequency and *ii*) polarization, *iii*) requirement of in-situ data, *iv*) backscattering model, *v*) and achieved performance. According to Ogen *et al.* [7] it is also possible to estimate near-surface soil moisture using soil reflectance across the visible and near-infrared (VIS-NIR-SWIR).

While passive microwave remote sensing allows only a coarse spatial resolution (*e.g.*, 25 – 50 km), active microwave remote sensing can provide medium-resolution (tens of meters) θ estimates. Higher spatial resolutions are achievable using active microwave only if acquired by airborne platforms because antennas are not yet sufficiently miniaturized to be installed on current Unmanned Aerial Systems (UAS).

Retrieving land surface characteristics with a hyper-spatial resolution [8] is possible in VIS-NIR-SWIR and thermal-infrared (TIR) regions of the electromagnetic spectrum using a new generation of calibrated sensors that can be installed on a UAS [9]. From these images, θ can be estimated by applying the “triangle” and “thermal inertia” methods.

The former has been used for both soil moisture and actual evapotranspiration estimation (see among others, [10] and [11], respectively). It examines the link between stomatal conductance and available water content by analysing the air-surface temperature difference versus the vegetation cover feature space. The triangular approach is widely applied in numerous studies to estimate θ , evaporative fraction, and vegetation drought stress across different ecosystems and regions using satellite or airborne data ([12]–[16]). Maltese *et al.* [17] developed a thermal admittance version of the triangle method by employing airborne images. Successively, the same research group applied the method on a diachronic basis [18]. Recently, Wang *et al.* [19] applied the triangle method to estimate θ with a high spatial resolution (at meter resolution) by employing images acquired by UAS.

Alternatively, the thermal inertia approach for the estimation of θ requires at least two thermal images and one shortwave image [20] to mimic the ability of the ground to accumulate heat during the day and release it during the night.

The applicability of these methods depends on the vegetation cover: the triangle method is in principle more suitable to be applied over vegetated soils than bare soils as it depends on the difference between air and underneath the canopy temperatures. This temperature difference depends on canopy stomatal resistance, which varies with soil water availability.

The thermal inertia is more suitable for bare soils as it is based on a one-dimensional thermal diffusion equation. The solution of this equation is obtained assuming that long-wave net radiation plus turbulent fluxes are linearly related to surface temperature [21]. These conditions are verified over bare soils or soils with low vegetation fractional cover [20]. Therefore, the triangle and thermal inertia methods have complementary fields of application. Some studies demonstrated that the triangle method infers on the vegetation stress which is mainly related to the θ availability especially in semi-arid area [18].

For this reason, the validation of θ estimated via the triangle method with in-situ measurements could not be achieved easily when other stress factors influenced the vegetation stress (including solar radiation, wind velocity, air humidity, and temperature).

Recently, Leng *et al.* [22] applied the Vegetation Index/Temperature (VIT) trapezoid scheme to calculate θ content over Moderate Resolution Imaging Spectroradiometer (MODIS) images using a pixel to pixel approach, wherein theoretical dry and wet edges were determined pixel-to-pixel using gridded meteorological datasets (at low spatial resolution, 0.0625°). As such, θ at dry and wet edges (at wilting point and field capacity) were calculated pixel to pixel using the clay and sand percentages according to Saxton and Rawls [23]. Other authors ([24], [25]) accounted for the different temporal dynamic of surface θ (controlled by evaporation) and root zone θ (controlled by transpiration) by suggesting a two-stage trapezoidal space approach, to model the difference in speed between vegetation and soil surface temperatures. Within the suggested approach, firstly, the lower space is driven by θ availability at the surface, subsequently; the upper space is driven by θ availability in the root zone.

On the other hand, outcomes of the thermal inertia over bare soil pixels could be directly validated with in-situ measurements collected with traditional techniques (*e.g.*, thermo-gravimetric method or TDR). However, the current available satellite or airborne thermal images are lacking a spatial resolution to adequately collect bare soil pixels.

Night time and daytime thermal imagery are available from few satellite and airborne platforms: for instance, Suomi National Polar-orbiting Partnership-Visible Infrared Imager Radiometer Suite (NPP-VIIRS) satellite sensor acquires Day/Night thermal images at 750m; Minacapilli *et al.* [26] obtained thermal inertia from ATM Daedalus 1268, that has an instantaneous field of view (IFOV) of 2.5 mrad capable of acquiring thermal images at 4 m spatial resolution to estimate θ over $110\times 90\text{ m}^2$ bare soil plot. These authors clearly showed

that the resolution scale is one critical parameter in evaluating the performance of the considered remote sensing approach.

In some cases, indeed, it could be appropriate to aggregate images to a lower spatial resolution so as to achieve the best correlation with in-situ measurements of θ [17].

In this paper, we take advantage of the hyper-spatial resolution provided by UAS (decametric resolution in this research) to select thousands of pixels where the hypotheses underlying the thermal inertia algorithm are fulfilled.

A simplified formulation of thermal inertia, the Apparent Thermal Inertia (*ATI*) method, is empirically calibrated to determine the spatial distribution of θ over the selected pixels. The spatial distribution of θ over a small field of interest is then achieved via a kriging interpolation process.

In the following, Section 2 introduces the theoretical background of the thermal inertia theory, Section 3 explains the methodology to estimate the soil moisture whether pixels are unshaded and bare or not, Section 4 describes the experimental site, Section 5 describes remotely sensed and in-situ data, Section 6 reports and discusses the results of the pre-processing (the empirical calibration of the *ATI* to estimate θ and the geostatistical analysis); all correlations shown in this section are classified according to Evans [27]. Finally, the concluding section (7) summarizes take-home messages, highlighting potentialities, limits of the method and suggesting a further improvement.

I. THEORETICAL BACKGROUND

The thermal inertia, P ($\text{J m}^{-2} \text{K}^{-1} \text{s}^{-1/2}$), represents the resistance of soil to temperature variations and it depends on the soil density and on two soil thermal properties, the specific heat and the soil thermal conductivity. All these variables are strongly influenced by θ . Specifically, soil thermal inertia increases as θ increases.

In this section, we discuss equations and variables relevant to the application of thermal inertia approach to map θ over small areas, such those usually acquired through fixed wings UAS. A more detailed description of the mathematical framework is given in the Appendix A1.

The estimation θ via thermal inertia theory is described in a pioneering and comprehensive paper from Price [28] accounting for the radiation budget at Earth's surface, including the turbulent heat fluxes.

To derive P from remote sensing, the 1D thermal diffusion differential equation is solved by imposing two boundary conditions, including the energy balance at the surface.

Under the hypothesis of bare or scarcely vegetated soils, the net longwave radiation minus sensible and latent heat fluxes of the surface energy balance are replaced by a linear form with the surface temperature according to Pratt *et al.* [21]. Thus, allowing explicitly solving the thermal diffusion equation.

Among others, Maltese *et al.* [29] tested the Pratt *et al.* [21] hypothesis on soil partially covered by vegetation (fractional cover up to ~ 0.5) verifying that modelled and *in situ* data are

still characterized by a strong relationship (coefficient of determination $r^2 \approx 0.86$).

The solution of the thermal diffusion equation is given via an n -order approximation Fourier series which describes the temperature fluctuation at a given depth and time. In the case of thermal images acquired during the increasing (or the decreasing) thermal transient a first order approximation should be adopted.

ATI (K^{-1}), is a simplified formulation of thermal inertia that accounts only for the daily surface temperature variation (determined by differencing of the two extreme surface temperatures) due to the incident solar radiation entering the soil through the co-albedo. Some studies have shown that *ATI* correlates well with the surface θ ([30]–[32]).

Thermal inertia, P , depends on *ATI*, on a multiplicative term A_1 , and on the phase shift δ_1 , and on the actual incident shortwave radiation reaching the soil, E_G (W m^{-2}), among other variables.

$$P = f(ATI, A_1, \delta_1, E_G). \quad (1)$$

This equation can be simplified under some hypotheses if applied over small areas as in the present case.

Firstly, it is assumed that E_G is constant within small areas such as those covered by a UAS flight. A raw characterization of the E_G spatial variability is reported in the study area section.

The characterization is based on the analysis of the *Regione Campania Assessorato Agricoltura* meteorological stations measurements (http://www.agricoltura.regione.campania.it/meteo/meteo_2018.html).

The term A_1 depends on the solar azimuth, ψ , as a function of the local latitude, α (2):

$$\psi = f(\alpha). \quad (2)$$

This term was included for applications at country or continental scales, and it can be considered as constants for small areas.

The spatial distribution of δ_1 (rad s^{-1}) could be obtained by processing three surface temperatures as proposed by Sobrino *et al.* [33]. According to Xue and Cracknell [34], a lumped value of δ_1 can be evaluated assuming that the time when the surface temperature reaches its maximum is constant over the whole study area.

According to Sobrino *et al.* [35], the absolute error of P using the lumped δ_1 (agreeing with Xue and Cracknell formulation, hereinafter referred to XC formulation) is similar to the one obtained with the three surface temperatures formulation, $\sigma = 50 \text{ TIU}$ ($\text{J m}^{-2} \text{s}^{-1/2} \text{K}^{-1}$) if the time of the maximum surface temperature is accurately known.

θ which is in principle derived via the so-called Kersten function (see equation A1.8 and A1.9) applied to P can be derived via the Kersten function applied to *ATI* directly.

Indeed, under the above mentioned hypotheses, the spatial distribution of ATI is thus proportional to the spatial distribution of P ; thus, it can be assumed that the Kersten function evaluated over P (see eq. A1.8) is almost equal to that evaluated over ATI , $K_P \cong K_{ATI}$ (see eq. A1.9).

This assumption was tested by Minacapilli *et al.* [26] during a laboratory experiment on different kind of soil. Results on Silty Clay soil were characterized by an $RMSE = 0.09$ (over clay $RMSE$ was 0.11).

In particular, once determined the spatial distribution of K_{ATI} , it is possible to estimate the values of θ through the

Murray and Verhoef approach (hereinafter, the MV approach) [36]:

$$\vartheta = f(K_{ATI}). \quad (3)$$

Noticeable, using the MV approach, Lu *et al.* [37] reported that the mean errors of estimated soil moisture is lower than $0.02 \text{ m}^3 \text{ m}^{-3}$.

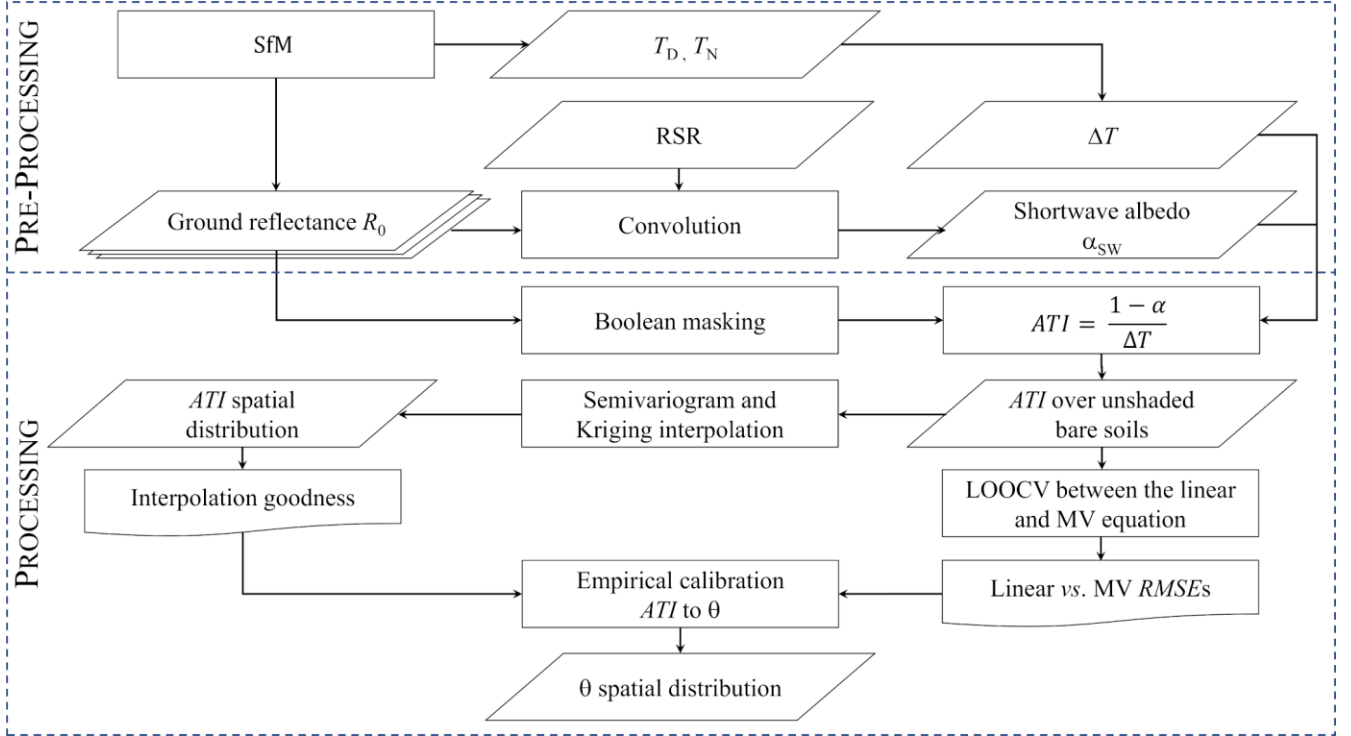


Fig. 1 Flowchart of the proposed method. The Structure-from-Motion (SfM) required in input night-time thermal images corrected with Radiometric Thermal Balancing (RTB), day-time thermal photographs and multispectral (MS) photographs in digital numbers (DN).

II. METHODOLOGY

The proposed method aims at estimating θ over both vegetated and shaded pixels. Fig. 1 depicts the chosen workflow, where the different steps are organized into pre-processing and processing phases. In the first phase, two input maps are obtained: the ΔT and the albedo. Then, these two maps are exploited in the subsequent phases to obtain the spatial distribution of θ .

The first part (A) of the method comprises in the pre-processing of the thermal input data; the second part (B) regards the empirical calibration of ATI function; finally, the third part concerns in the θ spatial distribution assessment via a geo-statistical approach.

Preliminary to these steps images need to be orthorectified using the Structure-from-Motion (SfM) technique ([38], [39]). While day-time thermal images required only orthorectification before the radiometric calibration and mosaicking, the night-time images required the additional

Radiometric Thermal Balancing (RTB), including a cross-track correction. The thermograph pre-processing (both methods and results) are reported in appendix A2.

After applying the cross-track correction, thermographs were mosaicked through the *Mosaicking tool* of ENVI 4.6.1 (Environment for Visualizing Images by Harris Geospatial Solutions, Inc.), by fixing the radiometric values of the central thermograph and adjusting the values of the other thermographs to match the fixed one (radiometric balancing).

A. Multispectral images pre-processing and Boolean masking

The multispectral image was calibrated in reflectance and corrected by the atmospheric effect through the empirical line method ([40], [41]). The linear relationship between DN at sensor level and spectral reflectance at ground level R_0 (–) calibrated for each band. To this aim, in-situ spectroradiometric acquisitions were collected over black grey

and white panels properly deployed in-situ during the UAS flights. In this step, the in-situ R_0 to be compared with DN of each band of the multispectral camera was determined considering the *Normalized Relative Spectral Response (RSR)* of the multispectral sensor.

Then, the shortwave albedo, α_{sw} (-), computed by weighting the ground reflectance spectral bands. Weights determined through a convolution, $RSR_{E_{sun}}$ ($W\ m^{-2}\ nm^{-1}$), between the *RSR* of the multispectral sensor and the solar irradiance [42]. Finally, the spatial resolution of α_{sw} was resampled to that of the thermal image through a *Pixel Aggregate* algorithm to calculate *ATI* (A1.7).

The thermal inertia hypotheses are fulfilled over bare or low vegetated soils, under the hypothesis that incident solar radiation follows cosine behaviour during diurnal hours. Thus, the *Random Forests* algorithm [43] was applied to classify bare-, shaded-, vegetated-, partially vegetated- pixels.

The classification training was carried out generating a number of training sites and dividing them into the four classes mentioned above. Then, a *Boolean* mask was extracted by isolating unshaded bare soil pixels from the others.

B. Empirical calibration of ATI to estimate θ

The *ATI* was calculated over unshaded bare soil by masking ΔT and α_{sw} . Then, in-situ θ measurements were compared to related *ATI* values with the aim of calibrating the *ATI* vs θ relationship. The first source of uncertainty is related to the best spatial resolution to be adopted for the subsequent spatial interpolation. To this aim, the *Leave-One-Out Cross Validation (LOOCV)* [44] was applied over some buffers around the θ measurement points with a gradually increasing diameter. For all in-situ measurement locations and corresponding buffer-diameters, the average values of *ATI* were compared to the in-situ θ measurements. The best spatial resolution was that leading to the highest determination coefficient, r^2 .

A second issue is about the model to be applied for estimating θ data based on *ATI*. Both linear regression and the MV formula were tested; the performance of both models was carried out in terms of *Root Mean Square Error (RMSE)* achieved by applying the *LOOCV*. The *LOOCV* was performed comparing the *ATI*-converted θ values and the in-situ θ (both thermo-gravimetric and TDR methods).

Low differences of RMSE indicate that linear regression can be employed for the conversion of *ATI* (as in our study case); alternatively, it is necessary to calculate the values of K_{ATI} (A1.10) from the *ATI* image and continue the analysis through the MV approach (A1.8).

C. Semi-variogram and kriging interpolation to map θ patterns

The interpolation of *ATI* allows estimating the thermal inertia of: *i)* actual vegetated soil with given amount of θ but without vegetation cover; *ii)* shaded pixels. Regarding the latter case, the actual inertia on vegetated soil, would produce an overestimation of θ , since net radiation is actually used also for latent and sensible heat fluxes and only partially not for

soil temperature variation through the ground heat flux. Regarding shaded pixels, remote estimation of *ATI* does not represent an accurate proxy of the thermal inertia, since would be assumed that the shortwave radiation reaching the ground, E_G , is uniform, and warms up the soil, while over shaded surfaces, losing heat to the atmosphere an exponential cooling occurs [e.g. [45], [46]].

Since the interpolation is not able to take into account the pattern of the vegetation density, hence the shielding of vegetation on the soil (both over vegetated pixels and shaded pixels), it produces a modelling mismatch that is quantified in the results section.

To interpolate the values of *ATI* of sparse not shadowed not vegetated pixels, the corresponding experimental variogram, $\hat{\gamma}(h)$, was computed (*Surfer 8* by Golden Software, LLC) by setting a maximum lag distance, h , approximately equal to the shorter length of the study area (100 m).

$$\hat{\gamma}(h) = \frac{1}{2n} \sum_{i=1}^n [\zeta(x_i) - \zeta(x_i + h)]^2, \quad (12)$$

where, ζ is the value of the attribute (*ATI* in the present research); x_i represents the pixel location, n accounts for the number of pairs of points separated by h .

A theoretical variogram was obtained by selecting variogram components (13) to be fitted to the empirical variogram.

Therefore, for each variogram component equation, some parameters were set by choosing the *least-squares* fit criterion [47]. Selected variogram components were: *i)* a *nugget effect model* calibrated by setting the *error*, C_0 , representing an offset; thus a measure of the direct repeatability of the measurements; *ii)* a *linear model* calibrated by setting the *slope*, S , representing the inclination of the variogram; *iii)* a *quadratic model* calibrated by setting the *scale*, C , and the *length*, a , which represent the height of the curve and the lag distance of the “knee”, respectively.

Variogram components equations	Model
$\gamma(h) = C_0$	Nugget effect
$\gamma(h) = S \cdot h$	Linear
$\gamma(h) = \begin{cases} \left(\frac{2 h }{a} - \frac{ h ^2}{a^2} \right), & \text{if } (h \leq a) \\ C, & \text{if } (h > a) \end{cases}$	Quadratic

(13)

Once fitted $\hat{\gamma}(h)$, with a theoretical model, $\gamma(h)$ (obtained by summing the different variogram components), it was possible to customize an *Ordinary Point Kriging* algorithm [48] to interpolate *ATI* (estimated over the unshaded non-vegetated pixels) over the whole study area. The spatial resolution, R_S , of the interpolation, was chosen equal to that resulting from the spatial resolution analysis (II, B). Furthermore, it needs to be assessed if the introduction of interpolated *ATI* over area shadowed and/or vegetated pixels decrease the r^2 values between measured θ and *ATI*, and to what extent.

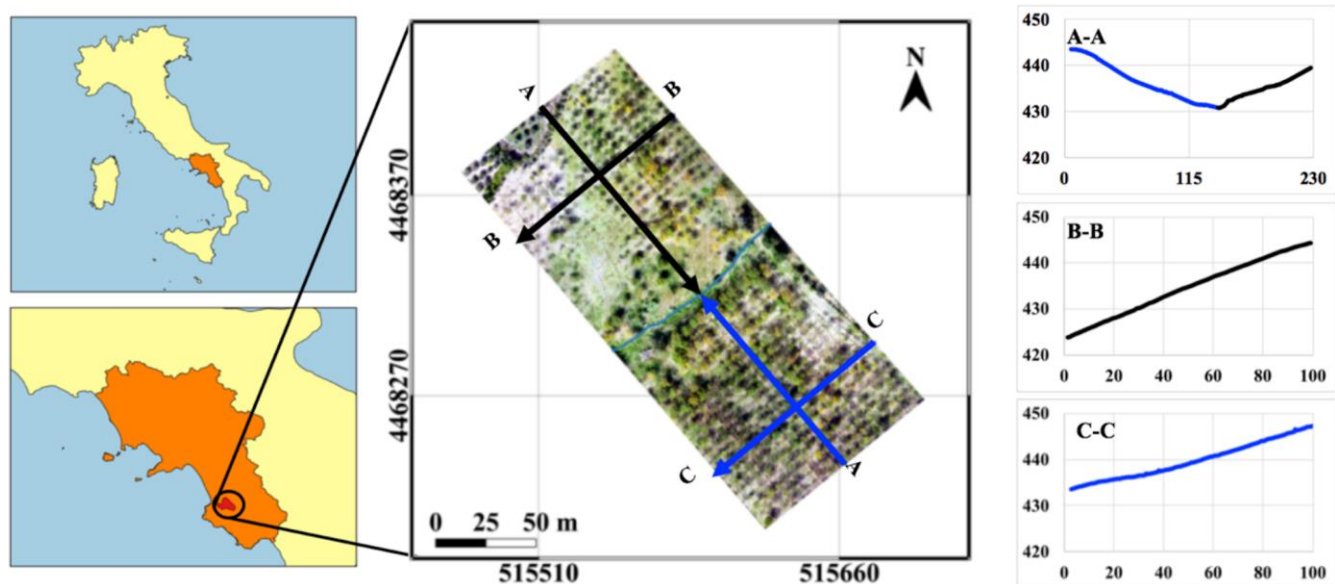


Fig.2 Location of the sub-catchment MFC2 (left panel, red polygon) in Campania (in orange), Italy (UTM WGS84 33N). Height profile of the middle section (A–A) orthogonal to the river average direction is represented in the top right panel. The height profiles of the middle sections parallel to the river direction are represented in the central and lower right panels. Blue lines represent the river left; black lines represent the river right.

To this aim, we created buffers with a diameter equal to the best spatial resolution around the θ measurement points, to estimate the average ATI within buffers overlaying pixels whether or not vegetates and/or shaded.

Under the hypothesis that the correlation remains strong, we can infer that it is reliable to obtain the spatial distribution of θ from interpolated ATI . The values of θ and ATI are related through a logarithm equation (MV approach). However, over a narrow range of variability of θ it could be simplified using a linear relationship. Nonetheless, this assumption needs to be tested.

III. STUDY AREA

The proposed method was applied over an experimental area belonging to the Alento River Catchment in the region of Campania (southern Italy). The Alento river is 36 km long and has its rise at about 900 m a. s. l. from Le Corne mountain near the village of Stio [49]. The experimental area is located within the sub-catchment named MFC2, which is located close to the village of Monteforte Cilento. Hereinafter, MFC2 will be used to indicate this experimental area.

The employed UAS surveyed the maximum rectangular flyable area in a single flight (with no batteries pack changes). The area extension was $\approx 100 \text{ m} \times 230 \text{ m}$ (Fig. 2), located at the average coordinate: 513580 East, 4468210 North in UTM WGS84 Zone 33N. A watercourse line (ephemeral creek) divides MFC2 from north-east to south-west (blue polyline in Fig. 2). The average slopes in the parallel direction are 21% and 16%, for the right and left sides (black and blue arrows in Fig. 2, respectively); while the average slopes perpendicular to the impluvium are $\approx 8\%$ and 12% for the right and left sides, respectively.

MFC2 represents a typical area where agroforestry is practised, with olive trees and a cherry orchard used for wood production. It is set on a regolith (matrix of silt and clay and a subordinate fraction of sand and gravel) above a turbidite argillaceous bedrock, with relatively low permeability ([50],

[51]). Details of the soil porosity, ϕ , at sample points in the study area are reported in Nasta *et al.* [52].

The variability of solar radiation during the acquisition day was about: -3.9 Wm^{-2} per 100 m of altitude ($r^2 = 0.5$) compared with an altitude range of $\approx 20 \text{ m}$, while the variability in North-South direction was -0.03 Wm^{-2} per 100 m ($r^2 = 0.35$) compared with a study area North-South extension of 230 m; finally, no trend was found in East direction ($r^2 \approx 0.01$).

IV. MATERIALS

A. Proximity sensing data

Day- and night-time thermal images were acquired from a UAS on the 3rd and 4th October 2018 at 14:00 and 6:00, local time respectively. The drone was programmed to acquire images following a double gridded flight pattern at a constant altitude of 70 m with 70% of front and side overlap and a speed of $6 - 7 \text{ ms}^{-1}$. This technique allowed to ensure proper overlap between images avoiding the presence of gaps and distortion during the total mosaic phase.

Acquisition times were properly selected: the diurnal images were acquired a couple of hours after noon thus maximizing the surface soil temperature and also minimizing shadows on both optical and thermal data; the night-time flight was performed at sunrise, with only diffuse radiation, thus minimizing the surface soil temperature and ensuring the absence of shadows in the acquired images. The UAS was a quadcopter Phantom 3 Professional (by DJI, Shenzhen, China). The imaging payload included a normal Red-Green-Blue (RGB) channel camera together with a thermal infrared camera or a multispectral camera mounted on a fixed support. The RGB camera is a 12.4 MP CMOS sensor (4000×3000 pixels). In addition, the UAS was equipped with a FLIR Tau2 336 thermal camera by FLIR Systems, Nashua, NH, USA (9 mm; F/1.25; Thermal Sensitivity: 50 mK) characterized by an image dimension of 336×256 pixels, a field of view (FOV) of

$35^\circ \times 27^\circ$ and an IFOV 1.9 mrad. This latter allowed to achieve a ground sampling distance (GSD) of approximately 0.15 m (Fig. 3a) for the thermal data.

The day-time multispectral image was acquired on the 3rd October 2018 at 15.00 local time by equipping the UAS with a Tetracam ADC Snap. The camera uses a 1.3 MPel electronic

global snap sensor that generates images consisting of 1280 x 1024 pixels; the FOV is $37.67^\circ \times 28.75^\circ$. At the flight altitude, the multispectral data had a GSD of approximately 0.05 m.

From the radiometric point of view, this camera acquires three bands with specific *RSRs* not representing the final NIR/Red/Green channels.

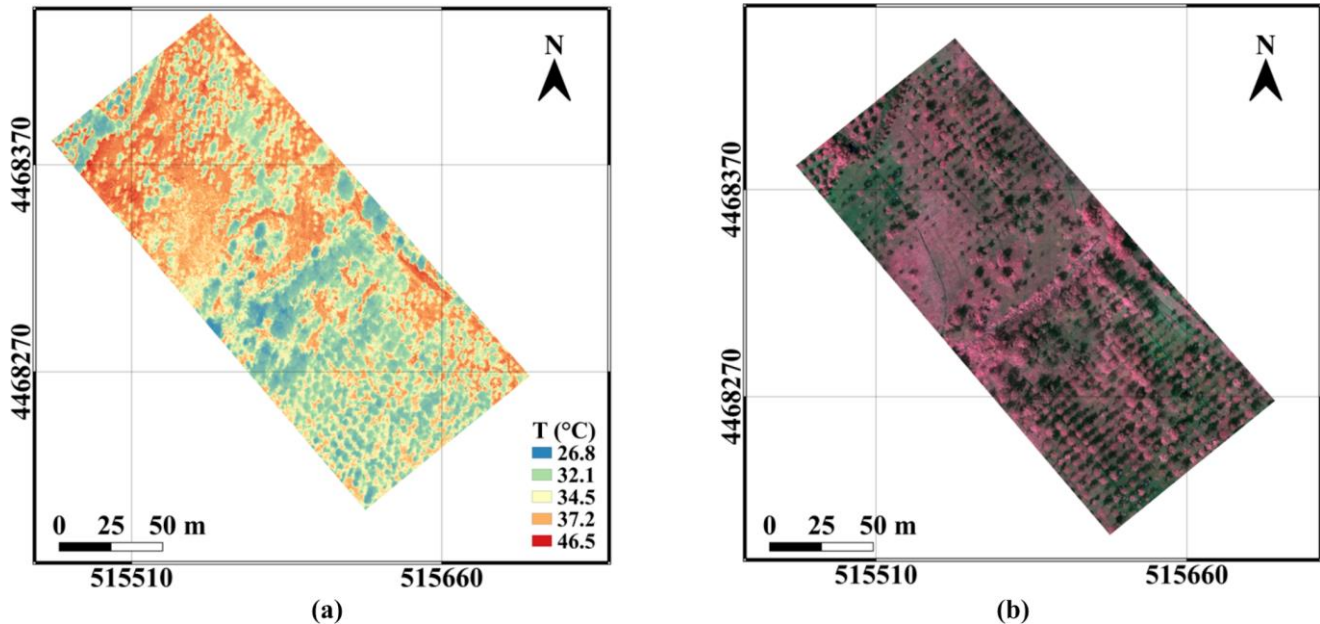


Fig. 3 Day-time thermal image (a) and multispectral image in Digital Number false-colour composition (NIR, R, G) (b).

Indeed, a blue absorbing glass filter is applied to remove the blue sensitivity from a channel measuring both in the blue and in the NIR spectra. Thus, the measured NIR is then subtracted from the green and the red bands using the image editing software PixelWrench2 (Tetracam Inc., Chatsworth, CA, USA) to produce the final NIR/Red/Green image (Fig. 3b).

B. In-situ data

Ground-based θ values were measured at twenty locations (Fig. 4), using both the thermo-gravimetric and TDR methods. Fourteen measuring points were identifiable in the UAS acquisition (not shadowed, not vegetated pixels).

Locations were selected according to the following main criteria: 1) to have soil moisture probes located on both sides of the small study catchment with respect to the ephemeral creek, and 2) to locate the sensors on a relatively regular grid over each side. Moreover, the entire catchment actually belongs to different landowners, and the sensors were located into the area where the landowner agreed to support our investigation.

The depth of measurement of the soil probes (0.15 m) was chosen to be comparable with TDR field measurements of surface soil moisture. The TDR instrument was a FieldScout TDR300 Soil Moisture Meter (by Spectrum Technologies, Inc.), characterized by a soil moisture resolution of 0.1%, with 0.15 m long steel rods.

The instrument has two Volumetric Water Content (VWC) modes: one for standard soils and one for higher clay soils. In each mode, the meter converts a measured electrical signal into volumetric θ using the Topp *et al.* equation [53]. The TDR-based θ , named θ_{TDR} in the remainder of this paper, was ranging between $0.07 \text{ m}^3 \text{ m}^{-3}$ and $0.24 \text{ m}^3 \text{ m}^{-3}$, while the average value was $0.16 \text{ m}^3 \text{ m}^{-3}$. The thermo-gravimetric-based θ , hereinafter named θ_{G} , was determined by using a standard laboratory protocol. Soil sampling was carried out by hand using a stainless steel core sampler with a plastic liner inside, with a length of 0.30 m and an inner diameter of 0.05 m. Each plastic liner was then cut into six pieces (each of 0.05 m length) to measure oven-dry soil bulk density and θ with the thermo-gravimetric method [52]. The wet weight was measured in-situ averaging three pieces of the sample, and the dry weight is obtained in the laboratory after oven-drying the remaining three pieces. Soil cores were then dried in the laboratory in a ventilated oven at 105°C for at least 24 h. The retrieved θ_{G} -data were ranging between 0.11 and $0.23 \text{ m}^3 \text{ m}^{-3}$, while the average value was $0.17 \text{ m}^3 \text{ m}^{-3}$. For the radiometric calibration of UAS optical images spectral signatures were collected through an FieldSpec Pro FR spectroradiometer (by ASD, Analytical Spectral Devices, Inc.) on dark and bright reference targets deployed on the study area during the UAS flights. The spectroradiometer allowed measuring reflected spectral radiances between 350 and 2500 nm. The instrument sampling interval is 1.4 nm for 350 – 1000 nm, 2 nm for 1000

– 2500 nm. The Spectral resolution is 3 nm @ 700 nm, 10 nm @ 1500 nm, and 10 nm @ 2100 nm. The wavelength accuracy is ± 1 nm.

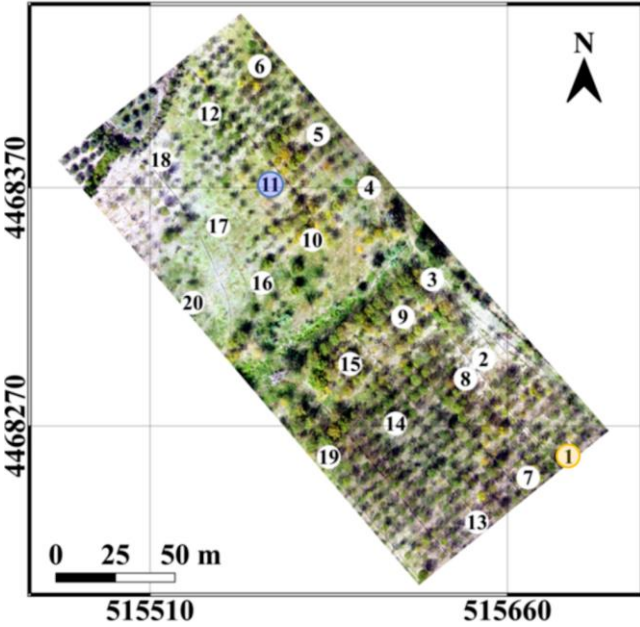


Fig. 4 Planimetric distribution of θ measurement points, overlaid to a true-colour representation of the study area.

The θ values collected overshadowed and/or vegetated pixels belong to the same population of those sampled over unshaded non-vegetated pixels: the Fisher statistic, F (0.01 and 0.17, for θ_G and θ_{TDR} , respectively) were lower than the critical value, $F_{crit} = 4.41$, in the analysis of variance (ANOVA) test [54]. The values of thermal diffusivity, D , were measured in-situ using a KD2Pro Thermal Properties Analyzer by Decagon Devices, Inc. (accuracy of $\pm 10\%$, at conductivities above $0.1 \text{ Wm}^{-1}\text{K}^{-1}$). Measurements were carried out in two points of the study area characterized by dry and wet conditions. These two measurements were almost co-located with θ sampling: point 1 for the dry condition (hatched in orange in Fig. 4) and point 11 for the wet condition (in blue in Fig. 4). The range of variability of z_d (damping depth) measured by the KD2Pro ranged between 11.6 cm and 9.10 cm (indirectly derived by the measured D spanning between $0.49 \text{ mm}^2 \text{ s}^{-1}$ and $0.31 \text{ mm}^2 \text{ s}^{-1}$).

V. RESULTS AND DISCUSSION

A. Multispectral image pre-processing and Boolean masking

The radiometric calibration to convert the DN acquired at UAS altitude into reflectance at the ground, R_0 , was carried out using the empirical linear method. In-situ ground reflectance to be used for the calibration of each spectral band

was obtained by the convolution of RSR of the camera with in-situ spectral reflectance.

The convolution between the RSR of the multispectral sensor and the solar irradiance provided three curves whose underlying areas are weights (0.39, 0.35 and 0.26 for the green, red and NIR band, respectively, Fig. 5a), which multiplied by R_0 provided the shortwave albedo, α_{SW} (Fig. 5c). The map of α_{SW} was resampled to the resolution of the thermal images (0.15 m) prior to calculating the ATI . A mask (Fig. 6a) for extracting unshaded non-vegetated pixels from α_{SW} and thermal images was obtained by applying a Random Forests classifier [43] to R_0 . Image of R_0 was classified in four classes: bare-, shaded-, vegetated-, partially vegetated- soil. Classified image was validated by generating 200 checkpoints using the Stratified Random [55] sampling method. The overall accuracy was 0.71: producer accuracies were 0.79, 0.77, 0.55 and 0.7 for bare-, shaded-, vegetated- and partially vegetated soil, respectively. The user accuracies were 0.90, 0.96, 0.65 and 0.37 for bare-, shaded-, vegetated- and partially vegetated soil, respectively. The Cohen coefficient was 0.61. After merging vegetated, partially vegetated and bare soil pixels to obtain a Boolean mask the overall accuracy rises to 0.92, the producer and user accuracy of the merged classes rise to 0.97 and 0.92, respectively. The Cohen coefficient rises to 0.78.

B. Empirical calibration of ATI to estimate θ

Once applied to the equation (A1.7), the ATI distribution over unshaded non-vegetated pixels were retrieved (Fig. 6b).

The first preliminary phase was to determine the best spatial resolution to be used for deriving the final θ map. This was achieved by comparing spatially averaged ATI with θ measured in-situ by considering a number of buffers of radius R_S around the measurement positions. The $LOOCV$ analysis revealed that the correlation gets higher concordantly with the detail of the raster images (Fig. 7) with its maximum ($r^2 = 0.67$) when pixel values are averaged over the smallest buffer (diameter of 0.15 m). While, using the whole dataset (thus including vegetated or shaded pixels) the correlation between ATI and θ_G was lower, ranging from $r^2 \approx 0.20$ to ≈ 0.23 (at $R_S = 0.15$ and 1.35 m, respectively).

Noticeably that, over pixels fulfilling the thermal inertia hypotheses, there is a comparable determination coefficient between in-situ gravimetric and TDR measurements ($r^2 = 0.77$), while it slightly decreases to $r^2 \approx 0.62$ using measurements over the whole dataset.

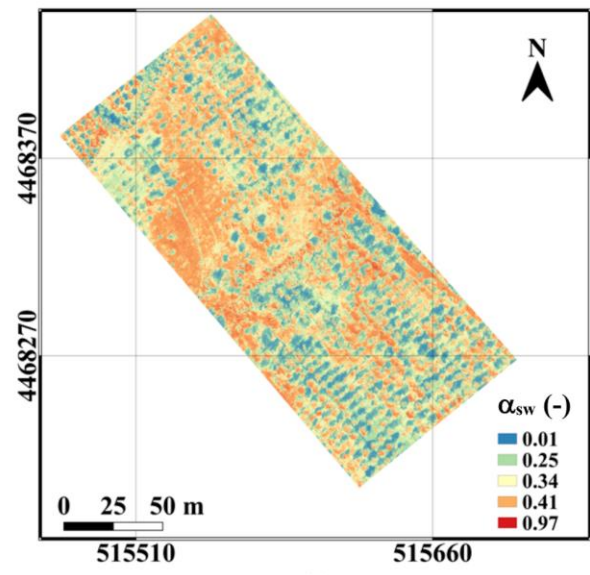
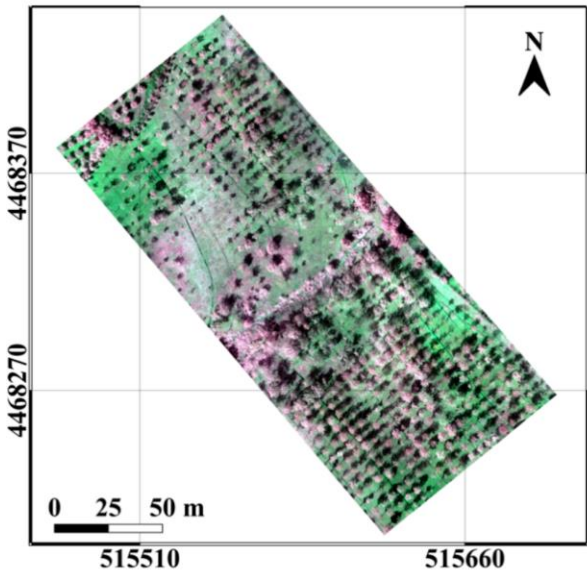
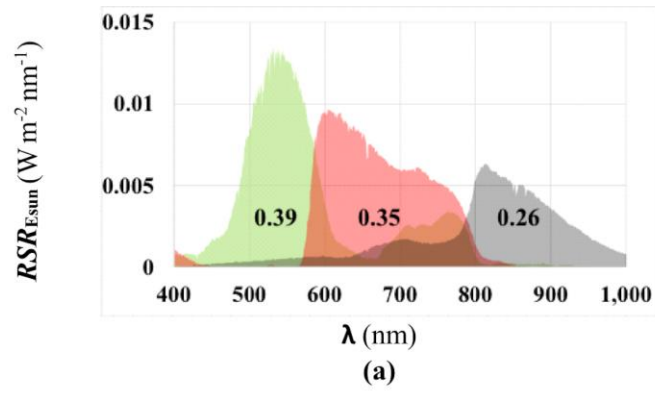


Fig. 5 Spectral variability of $RSR_{E_{sun}}$ (a) and map of R_0 in NIR, Red, and Green false-colour composition (b), and resulting α_{sw} (c).

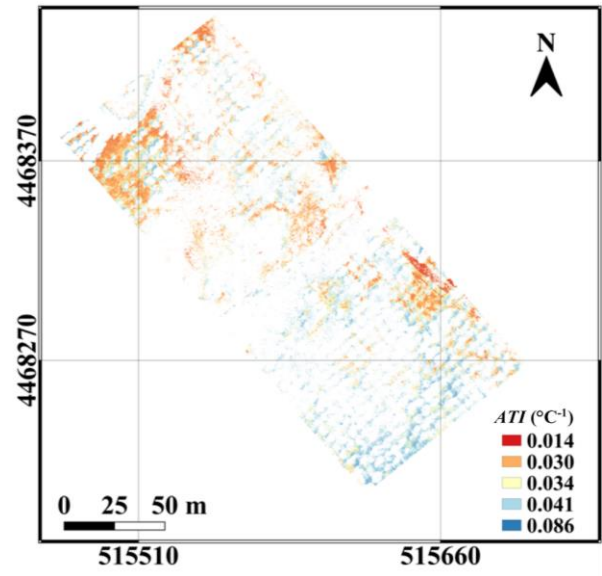
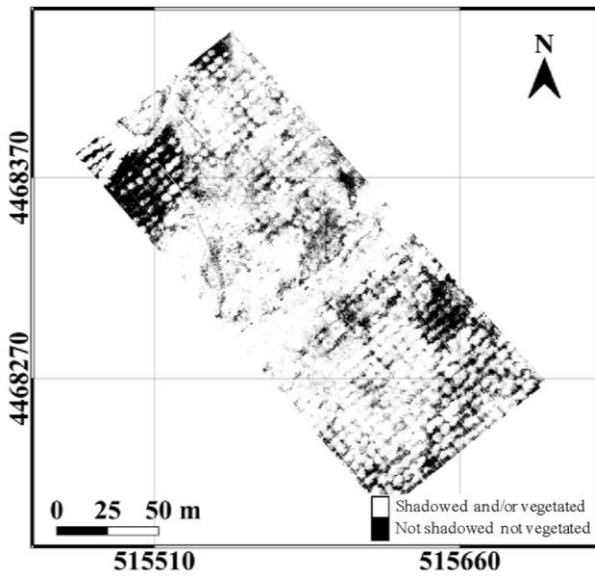


Fig. 6 Mask (a) used to extract ATI (b) over unshaded non-vegetated pixels.

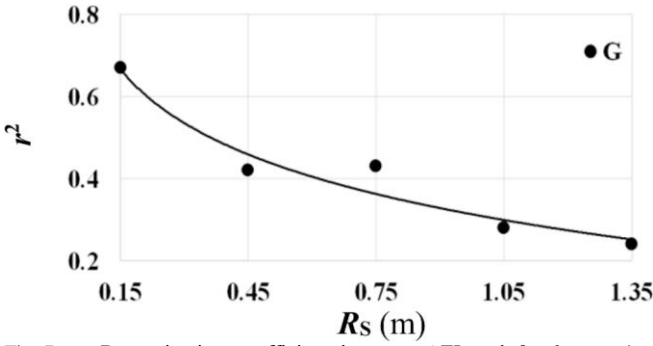


Fig. 7 Determination coefficient between ATI and θ_G for varying spatial resolution.

A second analysis was carried out to determine if, in the current case study, a linear relationship can be used to convert ATI to θ as the in-situ θ does cover a limited range of variability. The *LOOCV* analysis allowed to evaluate the agreement of estimated θ with in-situ ones using both the linear regression and the MV equation.

K_{ATI} versus θ_G relationship (Fig. 8, black line) is calibrated over unshaded non-vegetated points, a linear approximation (blue line) is also proposed for a limited range of variability of K_{ATI} . Comparing the linear and MV equations (Fig. 8), indeed, it is possible to notice that reliable results could be achieved using linear regression over a slightly wider K_{ATI} range ($K_{ATI} \approx 0.07 - 0.60$ which corresponds to $\theta \approx 0.08 - 0.29 \text{ m}^3 \text{ m}^{-3}$); out of this range, the relative error ($\varepsilon_R = 1 - \frac{\theta_{MV}}{\theta_L}$) considerably increases ($\varepsilon_R > 5\%$).

The linear regression between estimated θ and θ_G and θ_{TDR} allowed to achieve *RMSE* of $0.020 \text{ m}^3 \text{ m}^{-3}$ and $0.028 \text{ m}^3 \text{ m}^{-3}$ respectively; similar *RMSE* values were found ($0.020 \text{ m}^3 \text{ m}^{-3}$ and $0.029 \text{ m}^3 \text{ m}^{-3}$ corresponding to the gravimetric and *TDR*, respectively) by using the MV equation. Since there is a very low difference between the errors of the linear regression and the MV equation, we used the former to convert ATI to θ .

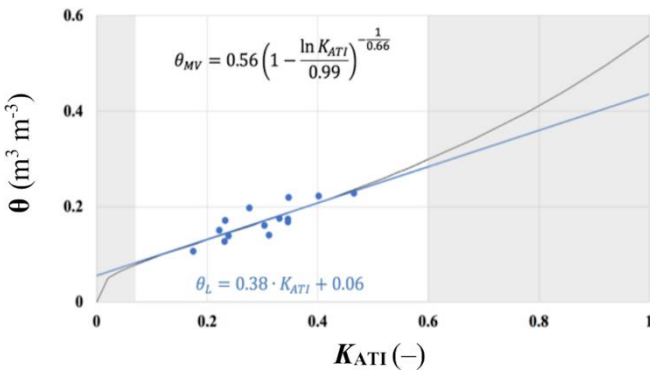


Fig. 8 K_{ATI} versus θ_G relationships following the MV approach (logarithm equation, in black) or a linear approximation (in blue). The grey bands indicate the range of K_{ATI} where $\varepsilon_R > 5\%$.

C. Semi-variogram and kriging interpolation

The ATI values over unshaded non-vegetated pixels were interpolated through a Kriging algorithm by calibrating a theoretical variogram over a maximum value of h equal to 100 m.

The theoretical variogram (Fig. 9c, blue points) results from the sum of three components whose parameters are calibrated to fit the empirical variogram (blue points). The values of the parameters of the variogram components are reported in Table 1: the parameter C_0 quantifies the *nugget effect*, and it was set to 1.4×10^{-5} ; the parameter S in the *linear* model was set to 2×10^{-7} ; the parameters C and a in the *quadratic* model were set to 3.2×10^{-5} and 25, respectively. Anisotropy ratio, A_R , is 2.0 and 1.6 for the linear and quadratic models, respectively; while, anisotropy angle, A_A , are 163° and 58° counter clockwise (CCW) from North for the linear and quadratic models, respectively.

The effect of anisotropy on h is clear when setting A_R different that unity only for the quadratic and the linear models, respectively (Fig. 9 a, b). The analysis highlights that the anisotropy parameters of the quadratic model are effective over the short distances ($h < 20$ m) where γ changes significantly with direction; while, anisotropy parameters in the linear model affect γ for $h > 20$ m. ATI was interpolated at 0.15 m spatial resolution (Fig. 9d).

To test the goodness of the method, the interpolated ATI average values inside the buffers of 0.15 m were compared to in-situ θ . As expected, r^2 decreased (Fig. 10) since measurements over vegetated and/or shaded pixels were included (red points): r^2 between ATI and θ_G was 0.59 (left panel) while it was 0.65 between ATI and θ_{TDR} (right panel). The slight decrease in r^2 (12% in terms of r^2 between ATI and θ_G) confirmed the appropriateness of the method. The θ_{TDR} values show a range of variability larger than θ_G .

Applying the linear equation to transform ATI to θ , it was possible to derive a continuous spatial distribution of θ in the study area, thus, providing values of this variable also in shaded and vegetated pixels (Fig. 11).

The offset between measured and estimated θ was almost negligible. Gain and *RMSE* allow evaluating under or over - estimations and the differences between sample values predicted by the ATI model θ_G and θ_{TDR} observed.

After Kriging interpolation, θ_G of bare soil was overestimated $\approx 0.1\%$ (with *RMSE* = $0.02 \text{ m}^3 \text{ m}^{-3}$), θ_G of vegetated soil were underestimated $\approx 5.5\%$ (with *RMSE* = $0.01 \text{ m}^3 \text{ m}^{-3}$). Overall, considering both bare soil and vegetated soil, θ_G was underestimated of $\approx 0.5\%$ (with *RMSE* = $0.02 \text{ m}^3 \text{ m}^{-3}$).

Analogously, θ_{TDR} of bare soil was overestimated $\approx 4.8\%$ (with *RMSE* = $0.02 \text{ m}^3 \text{ m}^{-3}$) θ_{TDR} of vegetated soil were underestimated $\approx 3.6\%$ (with *RMSE* = $0.02 \text{ m}^3 \text{ m}^{-3}$). Overall, considering both bare soil and vegetated soil, θ_{TDR} was overestimated of $\approx 3.8\%$ (with *RMSE* = $0.03 \text{ m}^3 \text{ m}^{-3}$).

The final map of UAS derived θ allows characterizing a day under the hypotheses underlying the thermal inertia method; while it does not take into account the hourly variability of θ .

Table 1 Parameters of the variogram components

Nugget Effect		Linear			Quadratic			
C_0	Micro	S	A_R	A_A	C	a	A_R	A_A
1.4×10^{-5}	0	2×10^{-7}	2.0	163	3.2×10^{-5}	25	1.6	58

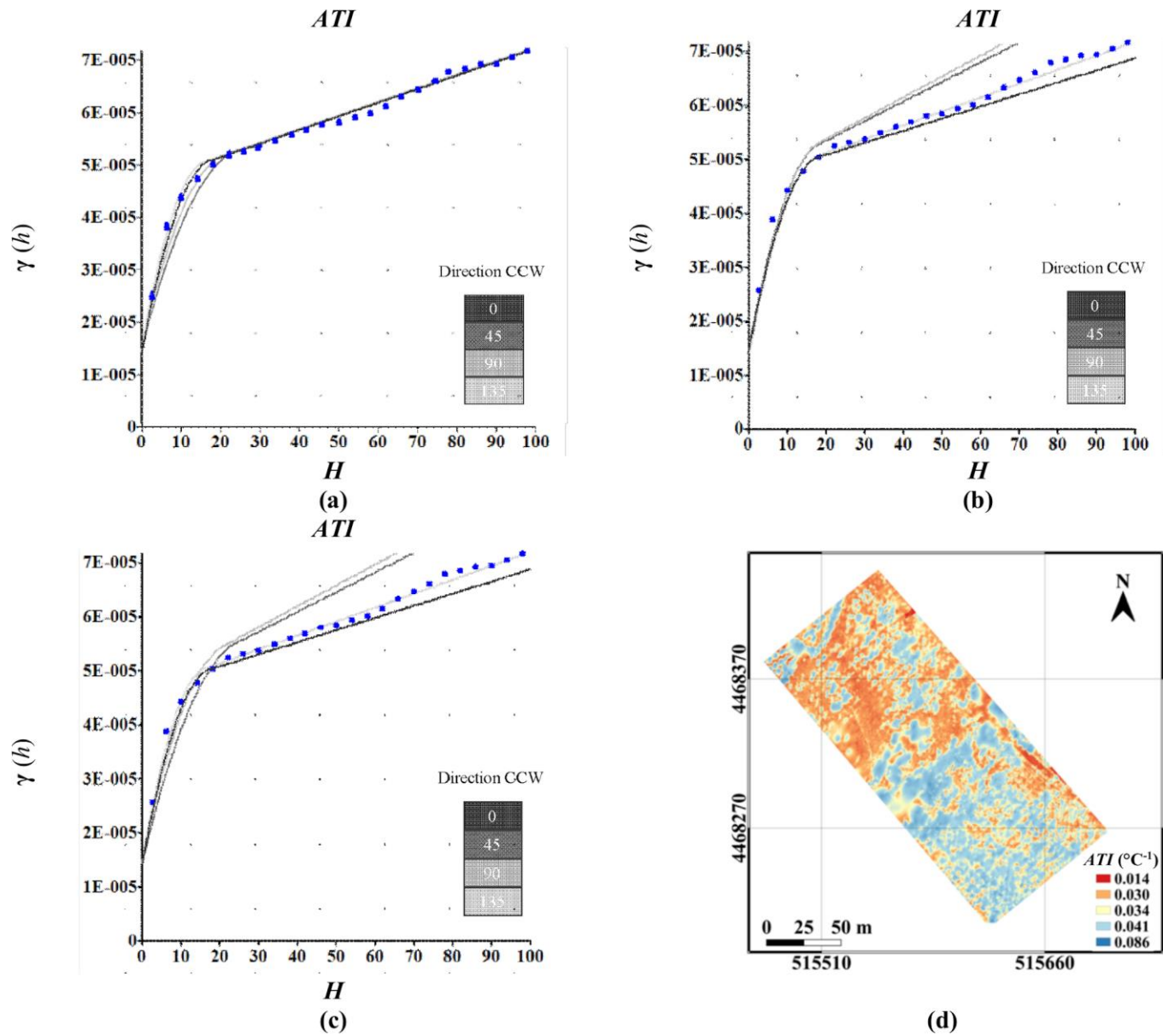


Fig. 9 Semi-variogram for varying anisotropy parameters of the quadratic model (a), for varying anisotropy parameters of the linear model (b). Adopted semi-variogram with varying anisotropy parameters of both quadratic and linear models (c) for the spatial interpolation of ATI (d).

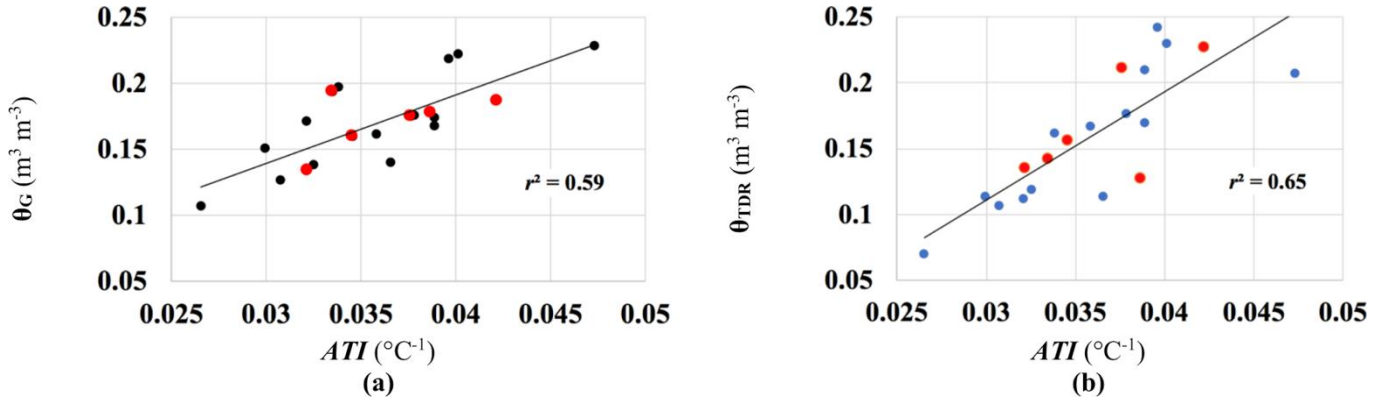


Fig. 10 Pairs of θ vs interpolated ATI over the whole measurement points: not shadowed not vegetated positions (in black or blue) and vegetated or shadowed positions (in red): (a) θ measured by gravimetric method; (b) θ measured by TDR method.

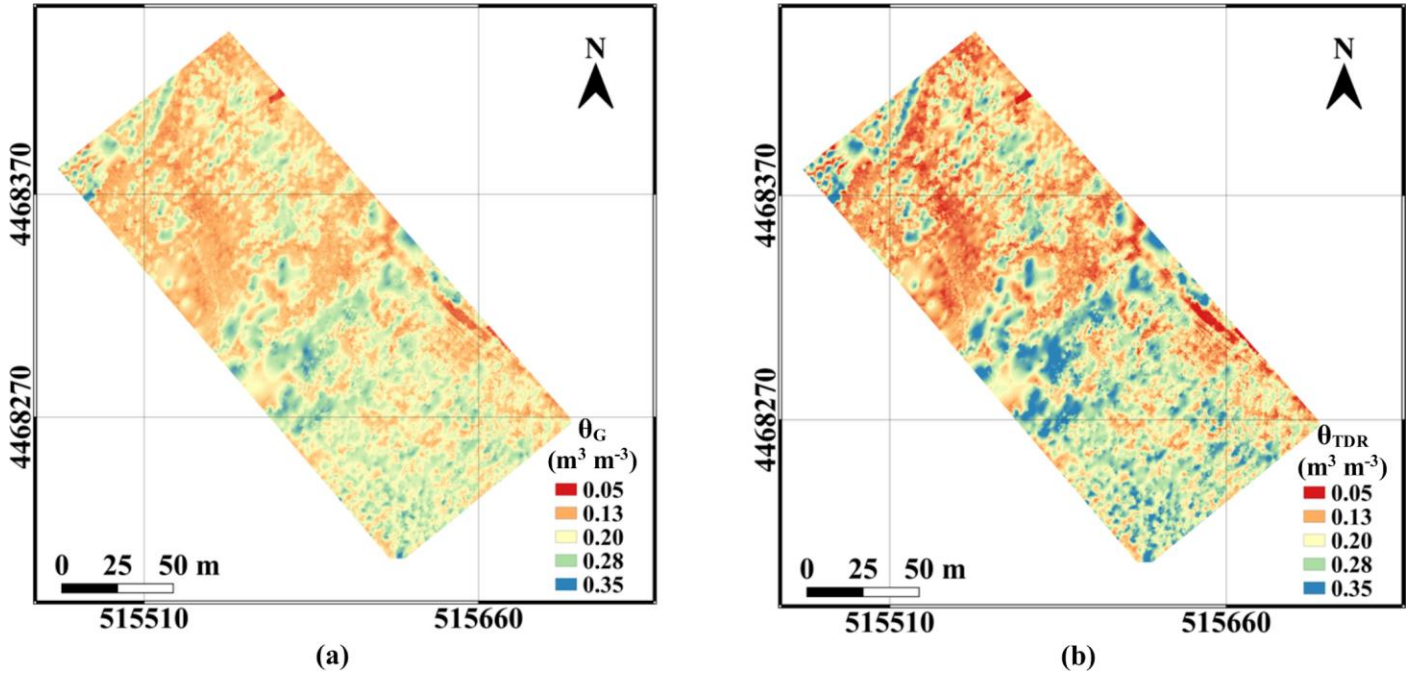


Fig. 11 Map of θ calibrated over gravimetric (a) and TDR (b) measurements.

VI. CONCLUSIONS

This study aimed at exploring the feasibility to implement a method to estimate soil water content from UAS images via the thermal inertia method. The applicability of the method was extended from unshaded non-vegetated pixels over vegetated and shaded pixels taking advantage of hyper-spatial resolution (0.15 m) offered by UAS acquisitions. The extension was possible by applying geostatistical analysis and interpolation over the pixels where the theoretical hypotheses are fulfilled. Indeed, the correlation between the soil water content dataset and the apparent thermal inertia over the whole measurement points was initially moderate ($r^2 \approx 0.2$, with θ_G as reference *in situ* data), but it was considerably higher over unshaded non-vegetated pixels ($r^2 \approx 0.7$).

We would emphasize that the hyper-spatial resolution offered by UAS-based acquisitions allowed to bridge a scientific gap. Indeed, these applications were carried out,

until now, using satellite or airborne remote sensing, and to maximize the correlation with in-situ θ was necessary to downscale the spatial resolution [17]; vice-versa, the use of hyper-spatial resolution images allow to fully exploit the potentiality of the thermal inertia method by selecting pixels where underlying hypotheses are fulfilled, and best accuracy is obtained at the highest spatial resolution.

The possibility to use linear regression to calibrate the apparent thermal inertia in soil water content was ratified using the *LOOCV* approach; it was also demonstrated that the linear model is still valid for a slightly larger range of variability of apparent thermal inertia and soil water content, within the range of in-situ measurements ($\approx 0.07 - 0.60$ for the apparent thermal inertia and $\approx 0.08 - 0.29 \text{ m}^3 \text{ m}^{-3}$ for the soil water content).

The application of the proposed method to the full range of variability of soil water content could be validated employing further in-situ data collection. In this case, it is evident that the

MV approach should be used to avoid relative errors $> 5\%$ instead of using the linear regression to calibrate the apparent thermal inertia *vs* the soil water content.

The analysis of the semi-variogram revealed that it is necessary to use a quadratic model for short lag distances (up to 25 m) and a linear model for larger lag distances (25 – 100 m) to interpret properly the variance of θ . Furthermore, a nugget effect model was applied to account for very short variability. Finally, the appropriateness of the proposed method was confirmed by the strong correlation found between the interpolated apparent thermal inertia and the gravimetric soil water content (*i.e.*, with a decreasing of only a 12% in terms of r^2).

For further improvement of the method, we suggest a technique to increase the numerousness of unshaded, not vegetated pixels. Since an orthomosaic is traditionally produced by using the nadir part of a photo/thermo-graph, and the numerousness of not vegetated pixels detected by a UAS change with the cameras acquisition geometry, we propose to generate additional orthomosaics using off nadir parts of the photo/thermo-graphs. However, directionalities effects, both in the reflective and emissive parts of the spectrum (see [56]) should be considered whether negligible or not.

APPENDICES

A1. THEORETICAL BACKGROUND

A1 reports the full equations of the theoretical background, while a list of the symbols used in this manuscript is reported in the Appendix A3.

P is defined as the square root of the specific heat, c ($\text{J kg}^{-1} \text{K}^{-1}$), by the thermal conductivity, K ($\text{W m}^{-1} \text{K}^{-1}$), by the soil density, d (kg m^{-3}): $P = (dcK)^{0.5}$. As discussed by Maltese *et al.* [29], the values of P from remote sensing can be evaluated from the equation:

$$P = \frac{(1-\alpha_{sw})E_G}{\Delta T} A_1 \frac{\cos(\omega t_1 - \delta_1) - \cos(\omega t_2 - \delta_1)}{\sqrt{\omega} \sqrt{1 + \frac{1}{b} + \frac{1}{2b^2}}}, \quad (\text{A1.1})$$

where, ω is the Earth rotational speed ($0.72 \times 10^{-4} \text{ rad s}^{-1}$), while the others variables of the equation are already defined in the previous sections of the manuscript. The equation terms can be obtained by processing three surface temperatures as proposed by Sobrino *et al.* [35]:

$$\delta_1 = \frac{(T_i - T_M)[\cos(\omega t_m) - \cos(\omega t_i)] - (T_m - T_i)[\cos(\omega t_i) - \cos(\omega t_M)]}{(T_m - T_i)[\sin(\omega t_i) - \sin(\omega t_M)] - (T_i - T_M)[\sin(\omega t_m) - \sin(\omega t_i)]} + (2m+1)\pi, \text{ with } m = 0, 1, 2, \dots, \quad (\text{A1.2})$$

where, T_M and T_m are two thermography characterized by a maximum and minimum surface temperatures (*e.g.*, at day and night time, respectively), T_i is intermediate thermography; t_M and t_m are the acquisition time of the maximum and minimum temperatures, respectively, t_i is the acquisition time of the intermediate thermography.

Thermal inertia equation (A1.1) is derived from the 1D thermal diffusion differential equation: $D \frac{\delta^2 T(z,t)}{\delta z^2} = \frac{\delta T(z,t)}{\delta t}$, by imposing two boundary conditions: a time constant temperature at infinite depth; the temperature fluctuations at the surface ($z = 0$) are exclusively dependent on the energy balance at the surface. Within the surface energy balance, the net longwave radiation minus sensible and latent heat fluxes are replaced by a linear form of the surface temperature.

The solution of the thermal diffusion equation is an n -order approximation Fourier series describing the temperature fluctuation at a given depth z and time t .

The approximation order of the Fourier series has to be chosen with care: a second-order approximation describes better the actual daily behaviour of the soil surface temperature, characterized by a steeper temperature variation during the increasing thermal transient, than that observable during the decreasing thermal transient; a first-order approximation should be suitable when all the thermal images are acquired during the increasing (or the decreasing) thermal transient.

The term b in equation (A1.1) depends on t_{\max} that is the time at which the surface temperature reaches the maximum (A1.3):

$$b = \frac{\tan(\omega t_{\max})}{1 - \tan(\omega t_{\max})}, \quad (\text{A1.3})$$

where, ωt_{\max} is the phase shift respect to the maximum reached by E_G , in the equation. (A1.1):

$$\delta_1 = \omega t_{\max}. \quad (\text{A1.4})$$

The equation (A1.4) is the so-called XC approximation [34], and it characterizes the study area independently of the acquisition time.

The equation (A1.1) can be simplified if we consider small areas.

Firstly, considering the ratio $C_1 = \frac{\cos \cos(\omega t_1 - \delta_1) - \cos \cos(\omega t_2 - \delta_1)}{\sqrt{\omega} \sqrt{1 + \frac{1}{b} + \frac{1}{2b^2}}}$, where both δ_1 and b , depend

on P . For small areas, this ratio can be assumed as a constant.

The term A_1 in equation (A1.1) depends on ψ measured counter-clockwise, and it is a function of the solar declination, δ_s , and α :

$$\psi = (\tan \delta_s \cdot \tan \alpha). \quad (\text{A1.5})$$

Therefore, the term A_1 is almost constant over small areas since it depends on α .

E_G is given by the irradiance reaching the soil reduced by a factor C_2 (the ratio between the actual and the theoretical solar irradiance reaching the soil for a given day) taking into account the cloud cover between the thermal acquisitions. Also, E_G varies only over large areas; thus, it can be assumed as a constant within areas covered by a UAS flight.

Summarizing, the P can be simplified as:

$$P = A \frac{1-\alpha_{sw}}{\Delta T}, \quad (\text{A1.6})$$

where the only spatially variable factor is defined as ATI (K^{-1}):

$$ATI = \frac{1-\alpha_{sw}}{\Delta T}, \quad (\text{A1.7})$$

and the scalar factor $A = C_1 E_C A_1$ includes the terms which can be considered as constant over small areas.

Once determined P , the MV approach [36] can be employed to estimate the θ (A1.8):

$$\theta = \phi \left(1 - \frac{\ln \ln K_p}{\varepsilon} \right)^{\frac{1}{\mu}}, \quad (\text{A1.8})$$

where, ϕ is the soil porosity, ε and μ are two shape parameters, set to 0.6 and 0.71, for fine-textured soils, respectively, and 2.95 and 0.16, for coarse-textured soils, respectively, while, K_p (–) can be expressed as (A1.9):

$$K_p = \frac{P - P_{dry}}{P_{sat} - P_{dry}}, \quad (\text{A1.9})$$

in which, P_{dry} and P_{sat} are the thermal inertia values of dry and saturated soils, respectively.

For operational applications, it is possible to calculate the Kersten function using the ATI , instead of P (A1.10):

$$K_{ATI} = \frac{ATI - ATI_{dry}}{ATI_{sat} - ATI_{dry}}, \quad (\text{A1.10})$$

where, ATI_{dry} and ATI_{sat} refer to the apparent thermal inertia values of dry and saturated soil, respectively. It is worth noting that $K_p = K_{ATI}$ when the δ_1 is calculated according to XC approximation.

The thickness of the investigated soil layer at which the maximum temperature excursion is e^{-1} , where e is Euler's number, of its value at the surface is called the damping depth, z_d [57]:

$$z_d = (2D\omega^{-1})^{0.5}. \quad (\text{A1.11})$$

It is a function of the soil thermal diffusivity, D ($\text{mm}^2 \text{s}^{-1}$) which, in turn, depends on θ ; D rules the heat diffusion into the soil profile and it is indicative of the penetration of the heat flux into the soil profile; thus, it influences the temperature oscillation at the soil surface ($z = 0$).

A2. THERMOGRAMS PRE-PROCESSING

Methods. The night-time thermograms were characterized by the temperature gradient, because the UAS was not equipped with a gimbal and the planned flight speed caused

the UAS to hold a tilted angle to compensate for the wind speed. At first, we applied a Cross-Track Illumination Correction algorithm [58] at the raw thermographs. The results of the algorithm depend on the scene itself, while we supposed that the temperature gradient resulted from the tilted position of the camera. Therefore, we calculated the average ratio between the “cross-tracked” and corresponding raw thermograms to obtain a multiplicative coefficient independent from the scene. As the analysis of northward and southward thermographs revealed only negligible differences, the RTB was applied independently from the flight direction through the use of an average multiplicative coefficient map.

Results. Night-time thermograms were characterized by a thermal trend both in descending and in ascending tracks (Fig. 12a and b, respectively).

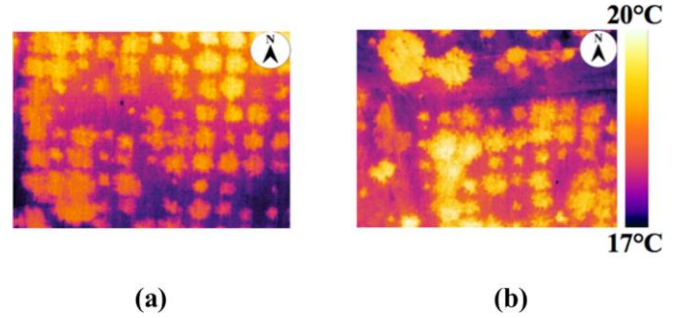


Fig. 12 Pseudo-colour representation of thermograms, highlighting a gradient of temperature in both descending (a) and ascending (b) tracks.

The trend was likely caused by the positive camera pitch angle during the tracks along the direction of forwarding motion as the UAS was not equipped by a gimbal. A multiplicative Cross-Track Thermal Correction (Fig. 13) was applied to remove the thermal trends within every thermogram both in the descending and ascending tracks.

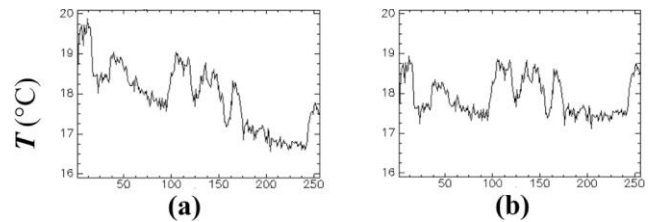


Fig. 13 Comparison between temperature profile before (a) and after (b) the application of Cross Track Thermal Correction for the descending thermogram in Fig. 6.

By relating the “cross tracked” thermograms to the raw thermograms, then dividing the results into the categories “ascending” and “descending”, negligible differences were found between ascending and descending correction parameters (Table 2). Therefore, it was decided to apply an average correction factor (a ramp image ranging approximately between 0.96 and 1.05). Corrected night-time thermograms were then mosaicked to obtain thermography of the whole study area (Fig. 14).

Table 2 – Statistics of the thermograms ratios

	Descending		Ascending	
	Min	Max	Min	Max
Max	0.99	1.07	0.97	1.08
Min	0.93	1.01	0.93	1.03
Average	0.96	1.04	0.96	1.05

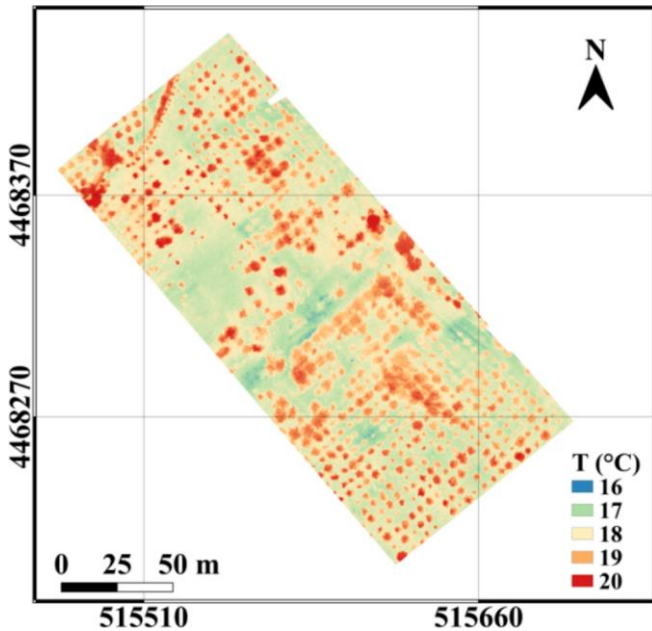


Fig. 14 Mosaicked night-time thermography.

A3. ACRONYMS USED IN THE MANUSCRIPT

Acronym	Meaning
ADC	Agricultural Digital Camera
ANOVA	Analysis of variance
ENVI	“Environment for Visualizing Image” software
FLIR System, Inc.	Forward Looking Infra-Red System Inc.
LOOCV	Leave One Out Cross-Validation
MFC2	Monteforte Cilento sub-catchment
MV	Murray and Verhoef approach
NIR	Near-Infrared
UAS	Unmanned Aerial System
RTB	Radiometric Thermal Balancing
TDR	Time Domain Reflectometry
TIR	Thermal Infrared
SAR	Synthetic Aperture Radar
SfM	Structure-from-Motion
UTM	Universal Transfer Mercator
VIS	Visible
VWC	Volumetric water content

A4. SYMBOLS USED IN THE MANUSCRIPT

Symbol	Meaning	Unit
α	Local latitude	($^{\circ}$)
α_{sw}	Short wave albedo	(–)
δ_1	Phase difference	(rad)
δ_S	Solar declination	($^{\circ}$)
ε	Shape parameter in Eq. (7)	(–)
ε_r	Relative error	(–)
μ	Shape parameter in Eq. (7)	(–)
φ	Soil porosity	(–)
$\hat{\gamma}$	Semi-variance in the experimental semi-variogram	K^2 in this application
γ	Semi-variance in the theoretical semi-variogram	K^2 in this application
θ	Soil water content on a volumetric basis	($m^3 m^{-3}$)
θ_L	θ calibrated using linear equation	($m^3 m^{-3}$)
θ_{MV}	θ calibrated using the MV approach	($m^3 m^{-3}$)
θ_G	θ from gravimetric	($m^3 m^{-3}$)
θ_{TDR}	θ from TDR	($m^3 m^{-3}$)
ω	Earth rotational speed	(rad s^{-1})
ψ	Solar azimuth	($^{\circ}$)
ζ	Attribute of the semi-variogram analysis	K^1 in this application
a	Height parameter in the quadratic γ model	(m)
A	Multiplicative scalar coefficient in Eq. (6)	($W m^{-2} s^{-1/2} rad^{-3/2}$)
A_1	Coefficient of the Fourier series in the first-order approximation	(rad $^{-1}$)
ATI	Apparent Thermal Inertia	(K^{-1})
ATI_{dry}	ATI over dry conditions (minimum value of ATI in the present case)	(K^{-1})
ATI_{sat}	ATI over saturated conditions (maximum value of ATI in the present case)	(K^{-1})
b	Coefficient in Eq. (1)	(–)
c	Soil specific heat	($J kg^{-1} K^{-1}$)
C	Scale parameter in the quadratic γ model	K^2 in this application
C_0	Error parameter in the nugget effect γ model	K^2 in this application
C_1	Multiplicative term in Eq (1)	($s^{1/2} rad^{1/2}$)
C_2	Cloud reduction coefficient of the daily incident irradiance	(–)
d	Soil density	($kg m^{-3}$)
D	Soil thermal diffusivity	($mm^2 s^{-1}$)
DN	Digital Number at the sensor level	(–)
E_G	Shortwave radiation reaching the soil	($W m^{-2}$)
f	Function of	
F	Fisher statistic	(–)
F_{crit}	Critical value of F	(–)
FOV	Field of View	($^{\circ}$)
IFOV	Instantaneous FOV	(mrad)
h	Lag distance	(m)
n	count of pairs of points separated by h	(–)
P	Thermal Inertia	($J m^{-2} K^{-1} s^{-1/2}$)
P_{dry}	P values of dry soil	($J m^{-2} K^{-1} s^{-1/2}$)
P_{sat}	P values of saturated soil	($J m^{-2} K^{-1} s^{-1/2}$)
K	Soil thermal conductivity	($W m^{-1} K^{-1}$)
K_{ATI}	Kersten function of ATI	(–)
K_P	Kersten function of P	(–)
r^2	Determination coefficient	(–)
R_0	Spectral reflectance at ground level	(–)
R_S	Spatial resolution and buffer diameter	(m)
RSR	Normalized Relative Spectral	(–)

	Response	
RSR_{Esun}	RSR and mean extra-terrestrial solar irradiance convolution	($\text{W m}^{-2} \text{nm}^{-1}$)
$RMSE$	Root Mean Square Error	$\text{m}^3 \text{m}^{-3}$ in this application ($\text{K}^{-2} \text{m}^1$, in this application)
S	Slope parameter in the linear γ model	()
t	Time	(s)
t_i	Acquisition time of T_i	(s)
t_m	Acquisition time of T_m	(s)
t_{max}	Time at which the surface temperature reaches the maximum	(s)
t_M	Acquisition time of T_M	(s)
T_i	Intermediate daily temperature	(K)
T_m	Minimum daily temperature	(K)
T_M	Maximum daily temperature unshaded not vegetated pixel	(K)
x	location (East, North) in the semi-variogram analysis	(m, m)
z_d	Damping depth	(m)
z	Soil depth	(m)

AUTHOR CONTRIBUTIONS

Methodology: A.P., F.C. and A.M.; software implementation: A.P.; results validation: A.P.; radiometric data acquisition and processing: A.P., E.B., N.F. and A.M.; images data acquisition and processing: A.P., F.C., S.M., S.F.D, R.Z. and A.M.; soil moisture data acquisition and processing: N.R., P.N.; soil thermal properties data acquisition and processing: Y.Z. and A.M.; writing—original draft preparation: A.P. and A.M.; writing—review and editing: A.P., G.C., F.C., S.M., S.F.D., R.Z., N.R., P.N., E.B., N.F., Y.Z. and A.M.; supervision: G.C., S.M., N.R., Y.Z. and A.M.

ACKNOWLEDGMENTS

The authors express their gratitude to the whole University of Naples Federico II team for technical support during the in-situ acquisition.

REFERENCES

- [1] N. Romano, 'Soil moisture at local scale: Measurements and simulations', *Journal of Hydrology*, vol. 516, pp. 6–20, 2014, doi: 10.1016/j.jhydrol.2014.01.026.
- [2] J. D. Bolten, W. T. Crow, T. J. Jackson, X. Zhan, and C. A. Reynolds, 'Evaluating the Utility of Remotely Sensed Soil Moisture Retrievals for Operational Agricultural Drought Monitoring', *IEEE Journal of Selected Topics in Applied Earth Observations and Remote Sensing*, vol. 3, no. 1, pp. 57–66, 2010, doi: 10.1109/JSTARS.2009.2037163.
- [3] I. Schröter, H. Paasche, P. Dietrich, and U. Wollschläger, 'Estimation of Catchment-Scale Soil Moisture Patterns Based on Terrain Data and Sparse TDR Measurements Using a Fuzzy C-Means Clustering Approach', *Vadose Zone Journal*, vol. 14, no. 11, p. vzj2015.01.0008, Nov. 2015, doi: 10.2136/vzj2015.01.0008.
- [4] S. Sabaghy, J. P. Walker, L. J. Renzullo, and T. J. Jackson, 'Spatially enhanced passive microwave derived soil moisture: Capabilities and opportunities', *Remote Sensing of Environment*, vol. 209, pp. 551–580, 2018, doi: 10.1016/j.rse.2018.02.065.
- [5] B. W. Barrett, E. Dwyer, and P. Whelan, 'Soil moisture retrieval from active spaceborne microwave observations: An evaluation of current techniques', *Remote Sensing*, vol. 1, no. 3, pp. 210–242, 2009, doi: 10.3390/rs1030210.
- [6] F. Capodici, A. Maltese, G. Ciruolo, G. D'Urso, and G. La Loggia, 'Power Sensitivity Analysis of Multi-Frequency, Multi-Polarized, Multi-Temporal SAR Data for Soil-Vegetation System Variables Characterization', *Remote Sensing*, vol. 9, no. 7, p. 677, Jul. 2017, doi: 10.3390/rs9070677.
- [7] Y. Ogen, J. Zaluda, N. Francos, N. Goldshleger, and E. Ben-Dor, 'Cluster-based spectral models for a robust assessment of soil properties', *Geoderma*, vol. 340, pp. 175–184, Apr. 2019, doi:

- 10.1016/j.geoderma.2019.01.022.
- [8] J. A. Greenberg, S. Z. Dobrowski, and S. L. Ustin, 'Shadow allometry: Estimating tree structural parameters using hyperspatial image analysis', *Remote Sensing of Environment*, vol. 97, no. 1, pp. 15–25, Jul. 2005, doi: 10.1016/j.rse.2005.02.015.
- [9] S. Manfreda *et al.*, 'On the use of unmanned aerial systems for environmental monitoring', *Remote Sensing*, vol. 10, no. 4, 2018, doi: 10.3390/rs10040641.
- [10] I. Sandholt, K. Rasmussen, and J. Andersen, 'A simple interpretation of the surface temperature/vegetation index space for assessment of surface moisture status', *Remote Sensing of Environment*, vol. 79, no. 2–3, pp. 213–224, 2002, doi: 10.1016/S0034-4257(01)00274-7.
- [11] R. Tang, Z.-L. Li, and B. Tang, 'An application of the Ts-VI triangle method with enhanced edges determination for evapotranspiration estimation from MODIS data in arid and semi-arid regions: Implementation and validation', *Remote Sensing of Environment*, vol. 114, no. 3, pp. 540–551, 2010, doi: 10.1016/j.rse.2009.10.012.
- [12] M. S. Moran, T. R. Clarke, Y. Inoue, and A. Vidal, 'Estimating crop water deficit using the relation between surface-air temperature and spectral vegetation index', *Remote Sensing of Environment*, vol. 49, no. 3, pp. 246–263, 1994, doi: 10.1016/0034-4257(94)90020-5.
- [13] T. N. Carlson, R. R. Gillies, and T. J. Schmugge, 'An interpretation of methodologies for indirect measurement of soil water content', *Agricultural and Forest Meteorology*, vol. 77, no. 3–4, pp. 191–205, 1995, doi: 10.1016/0168-1923(95)02261-U.
- [14] S. Stisen, I. Sandholt, A. Nørgaard, R. Fensholt, and L. Eklundh, 'Estimation of diurnal air temperature using MSG SEVIRI data in West Africa', *Remote Sensing of Environment*, vol. 110, no. 2, pp. 262–274, 2007, doi: 10.1016/j.rse.2007.02.025.
- [15] K. Mallick, B. K. Bhattacharya, and N. K. Patel, 'Estimating volumetric surface moisture content for cropped soils using a soil wetness index based on surface temperature and NDVI', *Agricultural and Forest Meteorology*, vol. 149, no. 8, pp. 1327–1342, 2009, doi: 10.1016/j.agrformet.2009.03.004.
- [16] M. Garcia, N. Fernández, L. Villagarcía, F. Domingo, J. Puigdefábregas, and I. Sandholt, 'Accuracy of the Temperature-Vegetation Dryness Index using MODIS under water-limited vs. energy-limited evapotranspiration conditions', *Remote Sensing of Environment*, vol. 149, pp. 100–117, 2014, doi: 10.1016/j.rse.2014.04.002.
- [17] A. Maltese, F. Capodici, G. Ciruolo, and G. Loggia, 'Soil Water Content Assessment: Critical Issues Concerning the Operational Application of the Triangle Method', *Sensors*, vol. 15, no. 3, pp. 6699–6718, Mar. 2015, doi: 10.3390/s150306699.
- [18] F. Capodici, C. Cammalleri, A. Francipane, G. Ciruolo, G. La Loggia, and A. Maltese, 'Soil Water Content Diachronic Mapping: An FFT Frequency Analysis of a Temperature–Vegetation Index', *Geosciences*, vol. 10, no. 1, p. 23, Jan. 2020, doi: 10.3390/geosciences10010023.
- [19] S. Wang *et al.*, 'Mapping root-zone soil moisture using a temperature-vegetation triangle approach with an unmanned aerial system: Incorporating surface roughness from structure from motion', *Remote Sensing*, vol. 10, no. 12, 2018, doi: 10.3390/rs10121978.
- [20] A. Maltese, F. Capodici, G. Ciruolo, and G. La Loggia, 'Mapping soil water content under sparse vegetation and changeable sky conditions: comparison of two thermal inertia approaches', *J. Appl. Remote Sens.*, vol. 7, no. 1, p. 073548, Jun. 2013, doi: 10.1117/1.JRS.7.073548.
- [21] D. A. Pratt, S. J. Foster, and C. D. Ellyett, 'A calibration procedure for Fourier series thermal inertia models.', *Photogrammetric Engineering and Remote Sensing*, vol. 46, no. 4, pp. 529–538, 1980.
- [22] P. Leng, Z.-L. Li, S.-B. Duan, M.-F. Gao, and H.-Y. Huo, 'A practical approach for deriving all-weather soil moisture content using combined satellite and meteorological data', *ISPRS Journal of Photogrammetry and Remote Sensing*, vol. 131, pp. 40–51, 2017, doi: 10.1016/j.isprsjprs.2017.07.013.
- [23] K. E. Saxton and W. J. Rawls, 'Soil water characteristic estimates by texture and organic matter for hydrologic solutions', *Soil Science Society of America Journal*, vol. 70, no. 5, pp. 1569–1578, 2006, doi: 10.2136/sssaj2005.0117.
- [24] H. Sun, 'Two-Stage Trapezoid: A New Interpretation of the Land Surface Temperature and Fractional Vegetation Coverage Space', *IEEE Journal of Selected Topics in Applied Earth Observations and Remote Sensing*, vol. 9, no. 1, pp. 336–346, 2016, doi: 10.1109/JSTARS.2015.2500605.
- [25] H. Sun, 'A Two-Source Model for Estimating Evaporative Fraction (TMEF) Coupling Priestley-Taylor Formula and Two-Stage

- Trapezoid', *Remote Sensing*, vol. 8, no. 3, Art. no. 3, Mar. 2016, doi: 10.3390/rs8030248.
- [26] M. Minacapilli, C. Cammalleri, G. Ciraolo, F. D'Asaro, M. Iovino, and A. Maltese, 'Thermal inertia modeling for soil surface water content estimation: A laboratory experiment', *Soil Science Society of America Journal*, vol. 76, no. 1, pp. 92–100, 2012, doi: 10.2136/sssaj2011.0122.
- [27] J. D. Evans, *Straightforward statistics for the behavioral sciences*. Pacific Grove: Brooks/Cole Pub. Co., 1996.
- [28] J. C. Price, 'THERMAL INERTIA MAPPING: A NEW VIEW OF THE EARTH.', *J Geophys Res*, vol. 82, no. 18, pp. 2582–2590, 1977, doi: 10.1029/JC082i018p02582.
- [29] A. Maltese, P. D. Bates, F. Capodici, M. Cannarozzo, G. Ciraolo, and G. La Loggia, 'Critical analysis of thermal inertia approaches for surface soil water content retrieval', *Hydrological Sciences Journal*, vol. 58, no. 5, pp. 1144–1161, 2013, doi: 10.1080/02626667.2013.802322.
- [30] T.-Y. Chang, Y.-C. Wang, C.-C. Feng, A. D. Ziegler, T. W. Giambelluca, and Y.-A. Liou, 'Estimation of root zone soil moisture using apparent thermal inertia with MODIS imagery over a tropical catchment in Northern Thailand', *IEEE Journal of Selected Topics in Applied Earth Observations and Remote Sensing*, vol. 5, no. 3, pp. 752–761, 2012, doi: 10.1109/JSTARS.2012.2190588.
- [31] M. Minacapilli, C. Cammalleri, G. Ciraolo, F. D'Asaro, M. Iovino, and A. Maltese, 'Thermal inertia modeling for soil surface water content estimation: A laboratory experiment', *Soil Science Society of America Journal*, vol. 76, no. 1, pp. 92–100, 2012, doi: 10.2136/sssaj2011.0122.
- [32] J. Qin, K. Yang, N. Lu, Y. Chen, L. Zhao, and M. Han, 'Spatial upscaling of in-situ soil moisture measurements based on MODIS-derived apparent thermal inertia', *Remote Sensing of Environment*, vol. 138, pp. 1–9, 2013, doi: 10.1016/j.rse.2013.07.003.
- [33] J. A. Sobrino and M. H. El Kharraz, 'Combining afternoon and morning NOAA satellites for thermal inertia estimation. 2. Methodology and application', *Journal of Geophysical Research Atmospheres*, vol. 104, no. D8, pp. 9455–9465, 1999, doi: 10.1029/1998JD200108.
- [34] Y. Xue and A. P. Cracknell, 'Advanced thermal inertia modelling', *International Journal of Remote Sensing*, vol. 16, no. 3, pp. 431–446, 1995, doi: 10.1080/01431169508954411.
- [35] J. A. Sobrino, M. H. El Kharraz, J. Cuenca, and N. Raissouni, 'Thermal inertia mapping from NOAA-AVHRR data', *Advances in Space Research*, vol. 22, no. 5, pp. 655–667, 1998, doi: 10.1016/S0273-1177(97)01127-7.
- [36] T. Murray and A. Verhoef, 'Moving towards a more mechanistic approach in the determination of soil heat flux from remote measurements. I. A universal approach to calculate thermal inertia', *Agricultural and Forest Meteorology*, vol. 147, no. 1–2, pp. 80–87, 2007, doi: 10.1016/j.agrformet.2007.07.004.
- [37] S. Lu, Z. Ju, T. Ren, and R. Horton, 'A general approach to estimate soil water content from thermal inertia', *Agricultural and Forest Meteorology*, vol. 149, no. 10, pp. 1693–1698, Oct. 2009, doi: 10.1016/j.agrformet.2009.05.011.
- [38] M. J. Westoby, J. Brasington, N. F. Glasser, M. J. Hambrey, and J. M. Reynolds, "'Structure-from-Motion" photogrammetry: A low-cost, effective tool for geoscience applications', *Geomorphology*, vol. 179, pp. 300–314, 2012, doi: 10.1016/j.geomorph.2012.08.021.
- [39] M. A. Fonstad, J. T. Dietrich, B. C. Courville, J. L. Jensen, and P. E. Carbonneau, 'Topographic structure from motion: A new development in photogrammetric measurement', *Earth Surface Processes and Landforms*, vol. 38, no. 4, pp. 421–430, 2013, doi: 10.1002/esp.3366.
- [40] E. Karpouzli and T. Malthus, 'The empirical line method for the atmospheric correction of IKONOS imagery', *International Journal of Remote Sensing*, vol. 24, no. 5, pp. 1143–1150, Jan. 2003, doi: 10.1080/0143116021000026779.
- [41] J. Kelcey and A. Lucieer, 'Sensor correction and Radiometric calibration of a 6-band multispectral imaging sensor for UAV remote sensing', 2012, vol. 39, pp. 393–398.
- [42] A. Palombo et al., 'Soil moisture retrieval by integrating TASI-600 airborne thermal data, WorldView 2 satellite data and field measurements: Petacciato case study', *Sensors (Switzerland)*, vol. 19, no. 7, 2019, doi: 10.3390/s19071515.
- [43] L. Breiman, 'Random forests', *Machine Learning*, vol. 45, no. 1, pp. 5–32, 2001, doi: 10.1023/A:1010933404324.
- [44] A. M. Molinaro, R. Simon, and R. M. Pfeiffer, 'Prediction error estimation: A comparison of resampling methods', *Bioinformatics*, vol. 21, no. 15, pp. 3301–3307, 2005, doi: 10.1093/bioinformatics/bti499.
- [45] M. J. Savage, 'Nowcasting daily minimum air and grass temperature', *Int J Biometeorol*, vol. 60, no. 2, pp. 183–194, Feb. 2016, doi: 10.1007/s00484-015-1017-7.
- [46] S. R. Singh and B. K. Sinha, 'Soil Thermal Diffusivity Determination from Overspecification of Boundary Data', *Soil Science Society of America Journal*, vol. 41, no. 5, pp. 831–834, 1977, doi: 10.2136/sssaj1977.03615995004100050002x.
- [47] D. L. Zimmerman and M. B. Zimmerman, 'A Comparison of Spatial Semivariogram Estimators and Corresponding Ordinary Kriging Predictors', *Technometrics*, vol. 33, no. 1, pp. 77–91, Feb. 1991, doi: 10.1080/00401706.1991.10484771.
- [48] N. Cressie, *Statistics for Spatial Data*. Wiley, 1993.
- [49] P. Nasta, M. Palladino, N. Ursino, A. Saracino, A. Sommella, and N. Romano, 'Assessing long-term impact of land-use change on hydrological ecosystem functions in a Mediterranean upland agroforestry catchment', *Science of The Total Environment*, vol. 605–606, pp. 1070–1082, Dec. 2017, doi: 10.1016/j.scitotenv.2017.06.008.
- [50] P. De Vita et al., 'Hydrogeology of continental southern Italy', *Journal of Maps*, vol. 14, no. 2, pp. 230–241, 2018, doi: 10.1080/17445647.2018.1454352.
- [51] N. Romano, P. Nasta, H. Bogena, P. De Vita, L. Stellato, and H. Vereecken, 'Monitoring hydrological processes for land and water resources management in a mediterranean ecosystem: The alento river catchment observatory', *Vadose Zone Journal*, vol. 17, no. 1, 2018, doi: 10.2136/vzj2018.03.0042.
- [52] P. Nasta et al., 'Integrating ground-based and remote sensing-based monitoring of near-surface soil moisture in a Mediterranean environment', in *2019 IEEE International Workshop on Metrology for Agriculture and Forestry (MetroAgriFor)*, Portici, Italy, Oct. 2019, pp. 274–279, doi: 10.1109/MetroAgriFor.2019.8909226.
- [53] G. C. Topp, J. L. Davis, and A. P. Annan, 'Electromagnetic determination of soil water content: Measurements in coaxial transmission lines', *Water Resources Research*, vol. 16, no. 3, pp. 574–582, 1980, doi: 10.1029/WR016i003p00574.
- [54] L. Støhle and S. Wold, 'Analysis of variance (ANOVA)', *Chemometrics and Intelligent Laboratory Systems*, vol. 6, no. 4, pp. 259–272, Nov. 1989, doi: 10.1016/0169-7439(89)80095-4.
- [55] R. G. Congalton, 'A review of assessing the accuracy of classifications of remotely sensed data', *Remote Sensing of Environment*, vol. 37, no. 1, pp. 35–46, Jul. 1991, doi: 10.1016/0034-4257(91)90048-B.
- [56] Zhang Renhua, 'A joint chain between thermal inertia model and geometric optical model of BRDF', in *IGARSS'97. 1997 IEEE International Geoscience and Remote Sensing Symposium Proceedings. Remote Sensing - A Scientific Vision for Sustainable Development*, Singapore, 1997, vol. 4, pp. 1956–1958, doi: 10.1109/IGARSS.1997.609164.
- [57] F. Quiel, 'THERMAL/IR IN GEOLOGY.', *Photogrammetric Engineering and Remote Sensing*, vol. 41, no. 3, pp. 341–346, 1975.
- [58] E. K. Robert, B. C. Warren, and T. Gen, 'Empirical methods to compensate for a view-angle-dependent brightness gradient in AVIRIS imagery', *Remote Sensing of Environment*, vol. 62, no. 3, pp. 277–291, 1997, doi: 10.1016/S0034-4257(97)00111-9.



of small lakes for floods

Antonio Paruta received a Master's degree in Land and Environmental Engineering from the University of Palermo (Italy) in 2019 discussing a thesis about a new technique to estimate soil water content through images acquired from Unmanned Aerial Systems (UAS). In 2020 received a scholarship from the University of Palermo within the project LIMNADI whose purpose is to use high spatial resolution images for the classification of lamination modelling.



Desertification” edited by the Italian Ministry for Environment.

Nunzio Romano received a M.Sc. degree cum laude in Civil Engineering. In 1990 he earned a Ph.D. in Hydraulic Engineering. In 2002, he was appointed Full Professor in Agricultural Hydraulics and Watershed Restoration. His area of research covers hydraulic engineering, soil hydrology, water resources management, irrigation and drainage. He worked with other experts on the report “National Communication to Combat Drought and



Harmonious Cost Action (<https://www.costharmonious.eu/>).

Giuseppe Ciraolo received his Ph.D. in hydraulic engineering from the University of Reggio Calabria (Italy) in the 2000. He is Associate Professor at the University of Palermo, teaching environmental remote sensing and coastal defence disciplines. He is author or co-author of more than 100 scientific papers. He is member of the management committee and responsible of the teaching activities of the



predictions under environmental changes – WATZON”.

Paolo Nasta completed his Ph.D. program in “Exploitation and management of agro-forestry resources” in 2009 at the University of Naples Federico II (Italy). He spent two years at University of Davis-California and two years at University of Lincoln-Nebraska with a post-doctoral position. He is currently a research assistant at University of Naples and local PI in the research project “WATER mixing in the critical ZONE: observations and



retrieval, Maltese et al. (2013)”.

Fulvio Capodici received a Ph.D. in hydraulic and environmental engineering from the University of Palermo (Italy) in 2010. His research field is Remote Sensing applied on Hydrology, Precision Farming, Sea Water Quality and Hydrodynamic fields monitoring by employing HF coastal radars. In 2015 he received the Tison Award 2015 for the paper “Critical analysis of thermal inertia approaches for surface soil water content



onboard the Intentional Space Station I 2022.

Eyal Ben-Dor is a full professor at the Tel Aviv University (TAU). Currently he is serving as the head of the remote sensing laboratory (RSL). He is an advisor for the SHALOM ASI-ISA mission to space and is a member of the advisory board of the Sentinel-10 mission on behalf of the European Space Agency (ESA, CHAIM mission). In addition he is a member of the EMIT- NASA scientific team mission to mount a hyperspectral sensor



soil moisture processes, vegetation patterns and UAS-based monitoring.

Salvatore Manfreda is Full Professor of Water Management, Hydrology and Hydraulic Constructions at the University of Naples Federico II. He is the Chair of the COST Action HARMONIOUS and the Scientific Coordinator of the Flood Forecasting System of the Basilicata Region Civil Protection. He has broad interest on distributed modelling, flood risk, stochastic processes in hydrology,



GIS, data analysis and soil sciences.

Nicolas Francos is a 2nd year PhD. student in hyperspectral remote sensing (HRS) at Tel-Aviv University (TAU). He holds a master degree with honours in geography with specialization in Geomatics from TAU. Nowadays, he is studying the gap between laboratory and field spectral observations of soil crust samples, evaluating the infiltration rate with the soil surface conditions. He is interested in remote sensing,



non contact techniques for environmental monitoring.

Silvano Fortunato Dal Sasso got his PhD in Methods and Technologies for Environmental Monitoring in 2012. He is PostDoc researcher at University of Basilicata and member the Hydrological LABORatory for Numerical Modelling and Advanced Environmental Monitoring (HydroLAB) research group. Currently, his main research activity aims to addressed to the use of UAS, satellite data and



of the HARMONIOUS Cost Action CA16219.

Yijian Zeng received the Ph.D. degree in vadose zone hydrology from the University of Twente (NL) in 2012, where he is currently working as an Assistant Professor (hydro-climatology). His current researches focus on developing the forward observation simulator, which integrates physically-based process models and microwave emission and scattering models. He is leader of WG3 ‘Soil Moisture’



the Use of Unmanned Aerial Systems for Soil Moisture Monitoring”.

Ruodan Zhuang received the M.Sc. degree in water resources and environmental management from ITC faculty of geo-information science and earth observation, University of Twente, the Netherlands, in 2018, and the bachelor's degree in hydrology and water resources engineering from Jilin University, China, in 2015. She is currently a PhD Candidate in University of Basilicata (DiCEM), Italy, with the research topic “On



Cost Action CA16219.

Antonino Maltese received a Ph.D. in hydraulic and environmental engineering from the University of Palermo (Italy) in 2008, where he works now as Assistant Professor (disciplines of Geomatics). In 2015 he received the Tison Award 2015 for the paper “Critical analysis of thermal inertia approaches for surface soil water content retrieval, Maltese et al. (2013)”. He is leader of the WG2 “Vegetation Monitoring” of the Harmonious